Spatial variations in the consolidation of sediments in the Neogene Miyazaki forearc basin, Southwest Japan

Yoshimoto, Takeru
Chiyonobu, Shun
Omori, Yasutomo
Zhang, Feng
Yamamoto, Yuzuru

(Citation)
Tectonophysics,862:229922

(Issue Date)
2023-09-05

(Resource Type)
journal article

(Version)
Accepted Manuscript

(URL)
https://hdl.handle.net/20.500.14094/0100483168

Spatial variations in the consolidation of sediments in the Neogene Miyazaki forearc basin, Southwest Japan

Takeru Yoshimoto[1]*, Shun Chiyonobu[2], Yasutomo Omori[3], Feng Zhang[4], Yuzuru Yamamoto[1]

([1]Kobe university, [2]Akita university, [3]JAMSTEC, [4]Nagoya Institute of Technology)

Abstract

The Neogene Miyazaki Group comprises forearc basin sediments exposed onland in South Kyushu in Southwest Japan, and is characterized by significant spatial variations in consolidation despite the minor differences in depositional ages. The Miyazaki Group is divided into three lithofacies (the Aoshima, Miyazaki, and Tsuma facies) from south to north. To evaluate the factors controlling lithification in the basin, the physical properties of the sedimentary rocks and the calcareous nannofossil biostratigraphy were investigated. The upper parts of the Aoshima and Miyazaki facies and the lower part of the Tsuma Facies were deposited at the same time (5–6 Ma), and have minor differences in maximum paleo-temperatures (97–116, 85–99, and 80–94°C, respectively), but major differences in porosity (15.9%, 25.5%–26.9%, and 26.1%–31.6%) and consolidation yield stress (38.2, 13.8–16.2, and 13.6–15.5 MPa). These findings indicate that the porosity reduction associated with consolidation is a more important control on the lithification than the depositional age and maximum temperature. There is a large difference in maximum burial depth between the Aoshima (>3500 m) and Miyazaki facies (<1600 m). It represents variations in sedimentary depositional environments in the Miyazaki Group: the Aoshima Facies were deposited in the deep-marine depocenter and deeply buried, whereas the Miyazaki and Tsuma facies were in the shallower marine facies and shallowly buried. After the deposition, only

the southern part of the Miyazaki forearc basin was largely uplifted, making distribution of the highly consolidated sedimentary rocks there. The large amount of uplift in the Aoshima Facies was apparently due to the subduction of the Kyushu–Palau Ridge beneath the forearc basin.

Keywords

Forearc basin; Miyazaki Group; Consolidation test; Vitrinite reflectance; Calcareous nannofossil; Lithification

1. Introduction

Consolidation of sediments is a key component of lithification in sedimentary basins. The porosity of clay-rich sediments is generally 75%–90% at the seafloor, and decreases to ~40% and ~10% at 500 and 4000 m below the seafloor, respectively, due to mechanical consolidation (Velde, 1996). As such, the porosity of sediments is used to constrain the diagenetic changes in a basin. The relationship between burial depth and physical properties (e.g., porosity, P-wave velocity, and shear strength) of sediments has been investigated using drillcore samples (e.g., Strasser et al., 2014; Tobin et al., 2015). Moreover, the consolidation state of sedimentary basins has been investigated by conducting consolidation tests on drillcore (e.g., Ask and Kopf, 2004) and outcrop samples (e.g., Uehara et al., 2016; Kamiya et al., 2017, 2020a).

Despite recent progress, lateral variations in lithofacies and the consolidation state of sedimentary basins are poorly understood. This is because drillcores represent one-dimensional information and cannot constrain spatial variations in the thickness and consolidation characteristics of sediments. Variations in sediment thickness along the sediment flow direction have been observed in forearc basins (e.g., Cornard et al., 2022), and affect the regional consolidation characteristics of a basin. Therefore, spatial variations in consolidation state need to be considered when

reconstructing the evolution of a basin.

In this study, we focused on the Miyazaki Group in a Neogene forearc basin in Southwest Japan (Fig. 1). The group comprises the Aoshima, Miyazaki, and Tsuma facies (from south to north). Despite minor differences in depositional ages, these facies exhibit major differences in their uniaxial compressional strength (Goto and Suzuki, 2011). Therefore, the Miyazaki Group is ideal for investigating lateral and vertical variations in the consolidation state and physical properties of sedimentary rocks in a sedimentary basin. We quantified the variations in consolidation from the porosity, consolidation yield stress, and maximum paleo-temperature. Calcareous nannofossil stratigraphy was also used to evaluate the effects of the depositional age on consolidation.

2. Geological setting

The Miyazaki area is located in the westernmost part of the Nankai Trough, where the Philippine Sea Plate is subducting beneath the Eurasian Plate (Fig. 1a). The Kyushu–Palau Ridge, which is a remnant arc on the Philippine Sea Plate, is subducting beneath the forearc accretionary wedge in the westernmost Nankai subduction zone (e.g., Park et al., 2009; Yamamoto et al., 2013; Zhang et al., 2020).

Late Miocene to Pleistocene forearc basin sediments (i.e., the Miyazaki Group; Fig. 1b) are widely distributed on the Miyazaki Plain and in mountains to the south, covering an area of 60 km from north to south, and 30 km from east to west. The Miyazaki Group unconformably overlies a Cretaceous to middle Miocene accretionary complex (i.e., the Hyuga and Nichinan groups) and middle Miocene silicic intrusive rocks (Fig. 1b), and is divided into three parts based on lithofacies (Shuto, 1952, 1961). The southern, central, and northern parts of the group are called the Aoshima, Miyazaki, and Tsuma facies, respectively. The Aoshima Facies (Fig. 2b) is characterized by alternating layers of highly lithified sandstones and mudstones. The Miyazaki

73 Facies (Fig. 2a) comprises moderately lithified sandstones and mudstones. The Tsuma Facies (Fig.
74 2a) comprises relatively poorly lithified sandstones and mudstones. Based on the stratigraphy, the
75 middle part of the Tsuma Facies (i.e., the Uryuno Formation) conformably overlies the upper
76 Miyazaki Facies (Fig. 2c; Kino et al., 1984; Endo and Suzuki, 1986). Each lithofacies in the
77 Miyazaki Group is >2000 m thick (Fig. 2c; Shuto, 1952, 1961; Kino, 1959; Kino et al., 1984;
78 Endo and Suzuki, 1986; Suzuki, 1987; Nakamura et al., 1999; Torii et al., 2000; Takashimizu,
79 2009; Oda et al., 2011). The mean orientation of bedding planes in the Aoshima, Miyazaki and
80 Tsuma facies is N20°E 21°E, N34°E 14°E and N27°E 10°E, respectively (Fig. 3). The dipping
81 angle of the Aoshima Facies is ~10° steeper than the Miyazaki and Tsuma facies.
82 The depositional age of the Miyazaki Group has been investigated by K–Ar dating of volcanic
83 tuffs, magnetostratigraphy, molluscan fossils, planktic foraminifera, and calcareous nannofossils
84 (Fig. 2c; Shuto, 1952, 1961; Endo and Suzuki, 1986; Suzuki, 1987; Ujiie and Oki, 1993;
85 Nakamura et al., 1999; Torii et al., 2000; Chiyonobu et al., 2011; Oda et al., 2011). The lower and
86 upper parts of the Aoshima Facies are assigned to the planktonic foraminiferal Zone N16 (Blow,
87 1969) and N17–N18, respectively (Nakamura et al., 1999). The Miyazaki Facies is assigned to
88 N17–N18 (Ujiie and Oki, 1993; Nakamura et al., 1999). Because the relationship between the
89 Aoshima and Miyazaki facies is unclear, two views regarding their age have been proposed: (1)
90 both are latest Miocene to Pliocene in age and accumulated during one transgressive period (Endo
91 and Suzuki, 1986; Ujiie and Oki, 1993); and (2) the top of the Aoshima Facies and bottom of the
92 Miyazaki Facies were deposited at the same time (Nakamura et al., 1999). The lower and upper
93 parts of the Tsuma Facies are assigned to N17–N18 and N18–N21, respectively (Suzuki, 1987).
94 K–Ar dating of volcanic tuffs in the lower, middle, and upper parts of the Tsuma Facies has
95 yielded ages of 6.2, 4.0, and 3.0 Ma, respectively (Fig. 2c; Torii et al., 2000). Therefore, the lower
96 parts of the Tsuma Facies (i.e., the Tsuma and Honjo formations) were deposited at the same time

as the upper Aoshima (i.e., the Aoshima Formation) and Miyazaki (i.e., the Ikime Formation) facies.

The Tsuma Facies is overlain by the Pleistocene Hyuga-nada Group across the Hisamine unconformity (Fig. 2c). The unconformity resulted from the tectonic activity associated with a change in the subduction direction of the Philippine Sea Plate from NNW to WNW at *ca*. 2.2 Ma (Oda et al., 2011).

3. Methods

3.1 Geological age based on calcareous nannofossils

Samples were collected from homogeneous and fresh siltstones in the Miyazaki Group. The sampling locations were the same for the porosity measurements and consolidation tests (Fig. 2). All samples were examined with a binocular microscope and prepared for calcareous nannofossil analysis using standard smear slide methods and optical adhesive as the mounting medium (Bown and Young, 1998). The calcareous nannofossils were analyzed under an optical polarizing microscope at 1500× magnification. The preservation state of the nannofossils was recorded following the criteria of Steinmetz (1979). Most Miocene and Pliocene datum described by Martini (1971) and Okada and Bukry (1980) have been identified in the sedimentary sequence. The absolute ages of the calcareous nannofossil biostratigraphy follow those proposed by Raffi et al. (2006).

3.2 Porosity

Homogeneous and fresh siltstone samples were collected from the Miyazaki and Hyuga-nada groups (Fig. 2). Initial sampling was conducted from outcrops, riverbeds, and coastal exposures using a chisel. The samples were cored perpendicular to the bedding plane using an electric-

121 powered drill with a coring bit (inner diameter, 27 mm). After coring, the samples were adjusted
122 to be 20 mm in height using an electric-powered rock saw. At least five specimens were prepared
123 and measured for each block.
124 The porosity of the siltstones was measured using the buoyancy method (Franklin, 1979). Firstly,
125 the saturated (M_{wet}) and submerged (M_{water}) weights of the cylindrical shaped specimens were
126 measured. After drying the specimens in an oven at 80°C for 5 days and cooling in a vacuum
127 desiccator to room temperature, the dry weight (M_{dry}) was measured.
128 The equation for calculating the porosity (ϕ) is as follows:

129 $$\phi = \frac{V_{void}}{V_{Bulk}} \quad (1)$$

130 $$V_{Bulk} = \frac{M_{wet} - M_{water}}{\rho_{water}} \quad (2)$$

131 $$V_{void} = \frac{M_{wet} - M_{dry}}{\rho_{water}} \quad (3)$$

132 where V_{Bulk} is the bulk volume of the specimen, V_{void} is the void volume of the specimen, and
133 the density of water was assumed to be 1.0 g/cm^3.
134 The equations for calculating the void ratio (e) and grain density (ρ_g) are as follows:

135 $$e = \frac{V_{void}}{V_{Bulk} - V_{void}} \quad (4)$$

136 $$\rho_g = \frac{M_{dry}}{V_{Bulk} - V_{void}} \quad (5)$$

137

138 **3.3 Vitrinite reflectance**

139 The thermal structure of the Miyazaki forearc basin was investigated using vitrinite reflectance
140 data (R_O). Vitrinite reflectance shows an exponential increase with increasing temperature from
141 50 to 300°C (e.g., Barker, 1983), and it records the highest temperature experienced by a sample.
142 Forty-two samples of sandstone and siltstone were collected (38 from the forearc basin and 4 from

143 the accretionary complex; see Fig. 2). The samples were crushed in a mortar and passed through
144 75–180 and 180–750 μm sieves under running water. For each sample, coal fragments were
145 separated and concentrated using heavy liquids (i.e., a sodium polytungstate solution with a
146 density of 1.8 g/cm^3). The separated grains were mounted in epoxy resin and polished using #1200,
147 #2400, and 0.06 μm alumina powder. The vitrinite reflectance measurements were conducted
148 following the method of Yamamoto et al. (2017). We used a silicon diode microphotometer with
149 546 nm non-polarized light and a focused beam of 1.6 μm in diameter. A total of 100 grains per
150 sample were measured in immersion oil (refractive index of 1.516), provided a sufficient number
151 of polished grains were present at the sample surface.
152

153 **3.4 Consolidation state**

154 In sedimentary basins, the consolidation of sediments proceeds only in the direction of gravity,
155 because lateral volume expansion is restricted by the surrounding rocks. This is called earth
156 pressure at rest (i.e., the K_0-condition; Jaky, 1944). During a consolidation test under K_0-
157 conditions, the void ratio of the sample decreases along with the consolidation stress (Fig. A1a in
158 the Appendix). Firstly, elastic deformation (i.e., over consolidation) proceeds under the stress state
159 that the samples have previously experienced. Secondly, the samples yield and plastic
160 deformation (i.e., normal consolidation) begins under the stress states that have not been
161 previously experienced. Therefore, the maximum effective stress is calculated as the
162 consolidation yield stress (p_c) from the consolidation curve.
163 In this research, consolidation tests were performed on siltstone samples using a uniaxial
164 consolidation testing method at a constant strain rate (Japanese Standards Association, 2009a, b).
165 The tests were conducted at the Nagoya Institute of Technology/JAMSTEC at a constant strain
166 rate of 0.01%/min and maximum vertical stress of 80 MPa under K_0-conditions. The details of the

apparatus were reported by Kamiya et al. (2017). The samples were surrounded by a rigid consolidation ring to restrict lateral volume expansion. To eliminate friction between the consolidation ring and sample, silicon grease sandwiched by two Teflon sheets was wrapped around the sample. To allow water to drain, filter papers and porous metal plates were placed on each end of the sample. The vertical load and displacement were measured and recorded at 1 Hz using a personal computer and data logger.

The samples were prepared from the same blocks as those used for porosity measurements. After coring perpendicular to the bedding, the diameters of the specimens were adjusted to fit inside the consolidation ring (25 mm) with two Teflon sheets, and one end surface was cut normal to the side of the cylinder using an electric-powered cylindrical grinder. The samples were then cut, and the cut surfaces ground down using an electric-powered surface grinder to make the cylinders 20 mm in height with parallel end surfaces. To avoid the development of excess pore water pressure in the specimens during the tests, the water saturation of the specimens was adjusted to 50% at room temperature before the tests.

The equation for calculating the void ratio e during the test is as follows, and ignores lateral volume expansion:

$$e = (1 + e_0)\frac{V_t}{V_0} - 1 \tag{6}$$

where e_0, V_0, and V_t are the initial void ratio, and the total volume of the specimen before and during the test, respectively. The mean void ratio calculated from the porosity measurements was used as e_0 for each sample.

Although many methods have been proposed to determine the value of p_c during consolidation tests (e.g., Casagrande, 1936; Janbu, 1969), most of these are subjective and suffer from scale dependence. In this study, we used the log–log method (Sridharan et al., 1991) to determine p_c, because this method is unaffected by the scale effect and is simple (Prakash and Sridharan, 2020).

The details of the log–log method are as follows (Fig. A1b in the Appendix).

(1) The consolidation curve is plotted on a log–log diagram showing the specific volume (1+e) and consolidation stress.

(2) Two straight lines are drawn, extending from the linear parts of the consolidation curve.

(3) The p_c value is defined as the stress at the intersection of the two straight lines.

Although the consolidation apparatus used in this study can apply a very high vertical load of up to 80 MPa for specimens of 25 mm diameter, the loading system is less accurate until the load exceeds 0.1 MPa. Therefore, in this study, line 1 of the log–log method was drawn based on the linear part of the consolidation curve at ~1 MPa. Line 2 was drawn in the highest stress area before unloading to limit the effects of cementation or strain softening (Kamiya et al., 2020b).

4. Results

4.1 Geological age based on calcareous nannofossils

The occurrences of calcareous nannofossils in each sample are summarized in Figure 4 and Table 1. *Discoaster berggrenii* and *Discoaster quinquerums* occur in samples MyCS1 and MyCS11 (Gonoharu Formation), MyCS2-2 (Tano Formation), and MyCS19 (Aya Formation). The occurrences of these species correlate with NN11 and CN9, and have ages of 8.52–5.59 Ma. Samples MyCS12-2 (Honjo Formation), MyCS13 (Uryuno Formation), and MyCS14 and MyCS18 (Tsuma Formation) are characterized by the occurrences of *Reticulofenestra pseudoumbilicus* and *Sphenolithus abies*, and the absence of *D. berggrenii* and *D. quinquerums*. The assemblages of samples MyCS12-2, MyCS13, MyCS14, and MyCS18 correlate with the interval from the last occurrence of *D. quinquerums* (5.59 Ma) to the last occurrence of *S. abies* (3.65 Ma). The last occurrence of *Discoaster tamalis* in samples MyCS9 and MyCS17

(Sadowara Formation) and MyCS22 (Ninazume Formation) defines the CN12a/b boundary (2.87 Ma). Therefore, these samples are 3.65–2.87 Ma in age.

Calcareous nannofossils are absent or occur infrequently in the upper Aoshima and Miyazaki facies. However, key species with the same biostratigraphic zonation occur in the lower Aoshima (Gonoharu Formation) and Miyazaki (Tano and Aya formations) facies. Ujiie and Oki (1993) reported the calcareous nannofossil and planktic foraminiferal zonation in the Miyazaki area. The upper Aoshima (Aoshima Formation) and Miyazaki (Ikime Formation) facies were deposited at the same time (5.82–5.59 Ma), based on the results of Ujiie and Oki (1993). Our results suggest that the lower Tsuma Facies (Tsuma, Honjo, and Uryuno formations) are 5.59–3.65 Ma in age. Torii et al. (2000) reported that deposition of the Tsuma Formation began at *ca*. 6.20 Ma, based on K–Ar dating (CBT-1; Torii et al., 2000). Therefore, the Aoshima and Ikime formations (5.82–5.59 Ma) can be correlated with part of the Tsuma and Honjo formations (6.20–3.65 Ma).

4.2 Porosity

There are wide variations in the porosity of siltstones in the Miyazaki Group (Fig. 5; Table 2). The porosity range of siltstones in the Aoshima Facies (12.1%–15.9%) is lower than that in the Miyazaki (21.6%–26.9%) and Tsuma (26.1%–45.5%) facies. The sandy siltstones (MyCS2, MyCS3, MyCS5, and MyCS6) have a relatively low porosity (14.3%, 21.1%, 17.5%, and 10.8%, respectively). The Hyuga-nada Group is characterized by high-porosity siltstones (43.7% ± 1.5%), similar to the top of the Tsuma Facies. In each lithofacies, the porosity of the siltstones decreases gradually from top to bottom, indicating that porosity reduction was related to burial. Samples with similar depositional ages have a similar porosity in the Tsuma (26.1%–31.6%; Tsuma and Honjo formations) and Miyazaki (25.5%–26.9%; Ikime Formation) facies, but a much lower

porosity in the Aoshima Facies (15.9%; Aoshima Formation). The grain density of siltstones in the Miyazaki forearc basin ranges from 2.64 to 2.73 g/cm^3 and is similar to that of siltstones in the Boso (2.60–2.70 g/cm^3; Kamiya et al., 2017) and Kumano (2.68 g/cm^3 at 950.5 mbsf; Tobin et al., 2015) forearc basins in central and offshore Southwest Japan, respectively. Therefore, the siltstones in the Miyazaki Group are representative of those in forearc basins, although there are major spatial variations in porosity between the three lithofacies.

4.3 Vitrinite reflectance and maximum paleo-temperatures

4.3.1 Vitrinite reflectance

Vitrinite reflectance show a normal distribution (Fig. 6). Some samples also contain grains with anomalously high reflectance that are derived from a highly mature source; consequently, the mean reflectance R_O (Fig. 4; Table 3) was calculated after such data were excluded.

Figure 7 shows the distribution of vitrinite reflectance values in the Miyazaki Group and the neighboring accretionary complex. The accretionary complex is characterized by high R_O values (0.84%–1.12%). The Miyazaki Group shows wide variations in R_O values (0.27%–0.73%). The mean vitrinite reflectance values in the Aoshima, Miyazaki, and Tsuma facies are 0.43%–0.73%, 0.40%–0.47%, and 0.27%–0.45% from top to bottom, respectively. The vitrinite reflectance increases gradually from top to bottom in each lithofacies, implying that the thermal maturity of the Miyazaki Group was affected by the general geothermal gradient. Samples with similar depositional ages have similar vitrinite reflectance values in the Tsuma (0.37%–0.45%; Tsuma and Honjo formations) and Miyazaki (0.40%–0.47%; Ikime Formation) facies, but slightly higher values in the Aoshima Facies (0.46%–0.58%; Aoshima Formation).

4.3.2 Maximum paleo-temperatures

Time-dependent models have been proposed to calculate the maximum temperature from vitrinite reflectance data (e.g., Sweeney and Burnham, 1990; Nielsen et al., 2017). We used the EASY%R_O program (Sweeney and Burnham, 1990) to calculate the maximum paleo-temperatures, based on the R_O values and burial history of each formation in the Miyazaki Group. In the program, different values of vitrinite reflectance are calculated by entering different burial histories and temperatures. The approximate depositional age was used to calculate the maximum temperature for each formation (Table A1). We assumed that heating in the entire Miyazaki forearc basin continued until *ca*. 2.2 Ma, corresponding to the development of the Hisamine unconformity. For example, the thermal history of the Aoshima Formation is as follows: (1) sediments accumulated on the seafloor at 5.5 Ma; (2) the sediments reached their maximum burial depth at 2.2 Ma; and (3) the sediments were uplifted to the surface at 2.0 Ma. Based on these burial histories, we determined the maximum paleo-temperature for each sample (Table 3).

The maximum paleo-temperatures in the Aoshima, Miyazaki, and Tsuma facies are 97–140°C, 85–99°C, and 46–94°C from top to bottom, respectively. Samples with similar depositional ages have similar maximum paleo-temperatures in the Tsuma (80–94°C; Tsuma and Honjo formations) and Miyazaki (85–99°C; Ikime Formation) facies, whereas the temperatures are 10–20°C higher in the Aoshima Facies (97–116°C; Aoshima Formation).

4.4 Consolidation state and maximum burial depth

4.4.1 Consolidation state

Figure 8 shows the consolidation curves for each sample. In all graphs, the linear part before yielding (over consolidation) is clearly observed. Some over consolidation curves for the Miyazaki and Aoshima facies appear to be non-linear, as their initial void ratio was low and the axes were enlarged in the early stage of the tests (Fig. 8e–f). After yielding, a linear trend (normal

286 consolidation) is clearly observed in the Tsuma Facies (Fig. 8a–c). Yielding behavior was
287 observed in the Miyazaki and Aoshima facies (Fig. 8d–f), but is relatively unclear. The
288 reproducibility of the consolidation tests for low-porosity siltstones was confirmed, using sample
289 MyCS4 (Fig. A2a in the Appendix). Two samples from the bottom of the Aoshima (MyCS1) and
290 Miyazaki (MyCS2) facies did not yield until 80 MPa (Fig. A2b in the Appendix).
291 Estimated p_c values (Table 2) of the Aoshima Facies are 48.4 and 38.2 MPa in its middle and
292 upper parts, respectively (Fig. 8f). Those of the Miyazaki Facies are 21.5–23.9 MPa (Fig. 8e) and
293 13.8–16.2 MPa (Fig. 8d) in its middle and upper parts, respectively. Those of the Tsuma Facies
294 are 15.5–16.4 MPa (Fig. 8c), 7.2–13.6 MPa (Fig. 8b), and 2.7–5.0 MPa (Fig. 8a) in its bottom,
295 middle, and upper parts, respectively. The p_c values increase gradually from top to bottom in each
296 lithofacies in the Miyazaki Group. The Aoshima Facies is characterized by the largest p_c value,
297 indicating that its maximum burial depth was greater than that of the Miyazaki and Tsuma facies,
298 given there was no excess interstitial pore fluid. Samples with similar depositional ages have
299 similar p_c values in the Tsuma (13.6–15.5 MPa; Tsuma and Honjo formations) and Miyazaki
300 (13.8–16.2 MPa; Ikime Formation) facies, but the p_c values are twice as large in the Aoshima
301 Facies (38.2 MPa; Aoshima Formation).
302
303 **4.4.2 Maximum burial depth and paleo-geothermal gradient**
304 We calculated the maximum burial depth (D_{max}) of the Miyazaki Group from the p_c values and
305 porosity/density as follows.
306 (1) The difference in burial depth between two samples (ΔD) was calculated from the difference
307 in the maximum effective stress (Δp_c):

308 $$\Delta p_c = (\rho_{bulk} - \rho_{water}) g \Delta D \quad (7)$$

309 where ρ_{bulk}, ρ_{water}, and g are the bulk sediment density, water density (1.0 g/cm^3), and

gravitational acceleration (9.8 m/s^2), respectively. ρ_{bulk} depends on the ratio of the pore space to the solid part of the sample (n) as follows:

$$\rho_{bulk} = (1 - n)\rho_s + n\rho_{water} \quad (8)$$

We assume that ρ_{bulk} is the mean value from two samples for which ΔD was calculated (Table A2a). For instance, the ρ_{bulk} of the overburden above MyCS17 (Sadowara Formation) was calculated using Eq. (8) and the mean n value of MyCS17 (Sadowara Formation) and MyCS15 (Takanabe Formation).

(2) To calculate D_{max} for each formation, we summed up ΔD as the overburden above the formation (Table A2a). For example, D_{max} for MyCS17 (Sadowara Formation) is the sum of ΔD for MyCS7 (Hyuganada Group), and MyCS15 (Takanabe Formation) and MyCS17 (Sadowara formation).

(3) The Miyazaki Facies is overlain by the Uryuno Formation (Fig. 2c). Because the top of the Miyazaki and Aoshima facies were deposited simultaneously, we assumed that the Aoshima Formation was also overlain by the Uryuno Formation or its equivalent. To calculate D_{max} for the Aoshima Facies, we assumed that the ρ_{bulk} value of the overlying sediment is the mean value for MyCS4 (Aoshima Formation) and MyCS13 (Uryuno Formation; Table A2c).

Table 2 provides the calculated D_{max} values for the Miyazaki Group. D_{max} ranges from 3590 to 4430 m from the upper to middle parts of the Aoshima Facies, 1390 to 2270 m from the upper to lower parts of the Miyazaki Facies, and 330 to 1630 m from the upper to lower parts of the Tsuma Facies. In the Tsuma Facies, D_{max} is consistent with the total stratigraphic thickness (Fig. 2c), considering the lateral variations in thickness. Moreover, there are wide variations in burial depth (>2000 m) between the Tsuma–Honjo (1370–1550 m), Ikime (1390–1600 m), and Aoshima (3590 m) formations, even though they were deposited at similar times.

Because samples from the Aoshima Facies (MyCS1, MyCS4, MyCS6, and MyCS11) have small

334 values of initial void ratios (<0.2), the consolidation curves might show faint yielding points (p_c).
335 To validate the results of the consolidation tests, we compared the stratigraphic thickness of the
336 Aoshima Facies (Fig. 2c) and calculated D_{max} from the consolidation tests (Table 2). For the
337 comparison, we constrained the paleo-geothermal gradient using the paleo-temperatures from the
338 vitrinite reflectance data and layer thickness data.
339 The paleo-geothermal gradient at the time of maximum burial of the Tsuma Facies was calculated
340 for two intervals (MyV10–MyV33 and MyV10–MyV42). Based on the stratigraphic thickness of
341 these intervals, the paleo-geothermal gradient is estimated to have been 26.7°C/km (MyV10–
342 MyV33) or 26.3°C/km (MyV10–MyV42). Based on the thickness of these intervals inferred from
343 D_{max}, the values are 28.8°C/km or 28.1°C/km, respectively.
344 The values of the Aoshima Facies were 17.3°C/km (between MyV7 and MyV11) or 16.7°C/km
345 (between MyV49-2 and MyV14) based on the stratigraphic thickness, and 17.8°C/km (between
346 MyV11 and MyV15, corresponding to MyCS4 and MyCS6) based on D_{max}. The paleo-
347 geothermal gradient based on differential D_{max} is similar to that based on stratigraphic thickness.
348 Therefore, the consolidation test data for samples with small void ratios (0.1–0.2) are valid.
349 The calculated paleo-geothermal gradient of the Tsuma Facies (26.3–28.8°C/km) is ~1.6 times
350 steeper than that of the Aoshima Facies (16.7–17.8°C/km). This variation can be explained by
351 variations in the thermal conductivity of the sediments. The heat flow Q (in mW/m^2) can be
352 expressed using the thermal conductivity κ (in W/mK) and geothermal gradient $\Delta T/\Delta d$ (in
353 K/km) as follows:

354 $$Q = \kappa \frac{\Delta T}{\Delta d} \quad (9)$$

355 When the heat flow is constant in an area, the geothermal gradient depends only on the thermal
356 conductivity of the sediments. In an experimental study using core samples from a modern forearc
357 basin, the thermal conductivity of mudstones increased from 1.5 to 2.2 W/mK with decreasing

porosity from 50% to 15% (Lin et al., 2020). Porosities of 50% and 15% correspond to those of the uppermost part of the Tsuma and Aoshima facies, respectively. Thus, it is reasonable that the paleo-geothermal gradient of the Tsuma Facies was ~1.5 times steeper than that of the Aoshima Facies.

5. Discussion

5.1 Controlling factors on lithification in forearc basins

Figure 9a–d shows the relationships between depositional age and porosity, maximum paleo-temperature, consolidation yield stress (p_c), and maximum burial depth (D_{max}), respectively. The depositional age is plotted as the age range for each sampling location, based on this and previous studies. The age ranges are summarized in Table A3 in the Appendix.

Gradual increase in the maximum paleo-temperature, p_c, and D_{max}, while gradual decrease in porosity with increasing depositional age, were identified in the Miyazaki Group (Fig. 9a–d). The porosity of the siltstones decreases linearly with increasing p_c (Fig. 9e), whereas there is little variation in the maximum temperature (Fig. 9f). Similarly, there are wide variations in p_c values (>20 MPa) between the Aoshima and other facies, despite the minor differences in maximum temperature (<20°C; Fig. 9g). Samples with similar depositional ages have major variation in p_c values (black arrows in Fig. 9). The Aoshima Formation has much larger p_c values (38.2 MPa) than the Ikime, Tsuma, and Honjo formations (13.8–16.2, 15.5, and 13.6 MPa, respectively). Although the maximum temperature of the Aoshima Formation (97°C) is higher than those of the Ikime, Tsuma, and Honjo formations (85–93, 94, and 80°C, respectively), the difference in temperature is small. Therefore, mechanical consolidation due to the maximum effective stress was the dominant control on lithification in this forearc basin, rather than depositional age or temperature.

382

383 **5.2 Sedimentary and burial history of the Miyazaki Group**

384 There is a large difference in maximum burial depth between the Aoshima and Miyazaki facies,
385 even though they have similar depositional ages (5–6 Ma). Although both facies show the similar
386 paleo-current direction (from NW to SE: Suzuki, 1987; Takashimizu, 2009), their sedimentary
387 environments were different. The depositional setting of the upper Aoshima Facies is considered
388 to have been a deep offshore basin (i.e., distal lithofacies), based on the presence of gravity flow
389 deposits (Ishihara et al., 2009). On the other hand, the Miyazaki Facies is considered to have
390 accumulated on a shallow marine to submarine slope (i.e., proximal lithofacies), based on benthic
391 foraminifera. Seismic data in Kumano forearc basin, Southwest Japan, supports the variations in
392 sediment thickness and burial depth along the direction of sediment flow (Cornard et al., 2022).
393 Thus, it is reasonable to infer that the Aoshima Facies had more potential for thicker sediment
394 accumulation than the Miyazaki Facies, and a maximum burial depth of the Aoshima Facies
395 (>3500 m) had been much greater than that of the Miyazaki Facies (<1600 m; Fig. 10a).
396 The depositional age of the lower Tsuma Facies is 6.2 Ma (K–Ar dating of tuff beds; Torii et al.,
397 2000) and it is assigned to planktonic foraminiferal Zone N17–N18 (Suzuki, 1987). This suggests
398 that the Tsuma Facies started accumulating at the same time as the upper Aoshima and Miyazaki
399 facies (Fig. 10a). Since *ca*. 5 Ma, both the upper Miyazaki (Ikime Formation) and middle Tsuma
400 (Honjo Formation) facies have been conformably overlain by the middle Tsuma Facies (i.e., above
401 the Uryuno Formation; Fig. 10b). This is evident from the similar p_c values of the Ikime and
402 Honjo formations (13.8–16.2 and 13.6 MPa, respectively). Figure 10b shows the maximum burial
403 depth of each lithofacies in the Miyazaki Group.
404

405 **5.3 Regional uplift associated with crustal tectonics**

406 In this study, we found that the maximum burial depth of the Aoshima Facies is greater than that
407 of the other facies despite the minor difference in the depositional ages. Sediments in the Aoshima
408 Facies were deeply buried (>3500 m) and tectonically uplifted, making distribution of the highly
409 consolidated sedimentary rocks only in the southern Miyazaki Group (Fig. 10e). Recent
410 topographic analyses of the paleo-shoreline and Quaternary terrace deposits unconformably
411 overlying the Miyazaki Group indicates the larger uplifting of the Aoshima Facies than the
412 Miyazaki and Tsuma facies (Nagaoka et al., 1991; 2010; Maemoku, 1992). The heterogeneous
413 uplifting in the study area is therefore still ongoing.
414 In addition, the Aoshima Facies forms in ~700 m-high mountains, whereas the other facies are
415 distributed on the Miyazaki Plain (lower than 200 m). Taking the present-day topography of the
416 region into account, the localized uplifting must have occurred in its southern part.
417

418 **5.3.1 Block rotation of the South Kyushu microplates**

419 The localized uplifting is supported by paleomagnetic studies. Paleomagnetic data for Miocene–
420 Pliocene sedimentary rocks from South Kyushu indicate that the region rotated ~30° counter-
421 clockwise with respect to the Eurasian continent during rifting of the continental crust beneath
422 South Kyushu and the northern Okinawa Trough (Kodama and Nakayama, 1993; Kodama et al.,
423 1995). Southeast Kyushu is divided into three microplates (Fig. 10c) during the period of the
424 rotation (Kodama et al., 1995). The boundary between two of the microplates corresponds to the
425 boundary between the Aoshima (block B in Fig. 10c) and Miyazaki (block A in Fig. 10c) facies,
426 which is characterized by intense seismicity and sinistral focal mechanisms (Kagiyama, 1994).
427 Paleomagnetic mean direction of the Aoshima Facies is D (declination) = 322.0° and I
428 (inclination) = 48.6° (Kodama and Nakayama, 1993), whereas those of the Miyazaki and Tsuma
429 facies are D = 338.6° and I = 47.5° (Kodama et al., 1995). It suggests that the Aoshima Facies

rotated ~16° counter-clockwise with respect to the Miyazaki and Tsuma facies. Therefore, the Aoshima Facies was isolated from the northern Miyazaki Group due to the block rotation and tilted more than the northern part (Figs. 3 and 10d). Thus, the rotation of South Kyushu apparently related to the independent crustal uplifting of the Aoshima Facies.

5.3.2 Subduction of the Kyushu–Palau Ridge

Seismic images of Pacific subduction zones and numerical experiments of forearc regions suggest that the forearc uplift is generally caused by tectonic underplating of subducting slabs (e.g., Menant et al., 2020; Scholl, 2021). The heterogeneous underplating beneath the study area that is for example, if the thicker input of sediments or topographic high were underplated beneath the Aoshima Facies, localized uplifting should be explained. The subducting Kyushu–Palau Ridge is the most prominent topographic characteristics in South Kyushu since the latest Miocene (Mahony et al., 2011), which can make the major variation in the forearc uplift.

There are some evidences showing the subduction of the Kyushu–Palau Ridge; negative free-air gravity anomalies, low seismic velocity anomalies, and a seafloor topographic bulge are characterized in the forearc extension of the Kyushu–Palau Ridge (e.g., Nawa et al., 2005; Tahara et al., 2008; Park et al., 2009; Yamamoto et al., 2013, Xia et al., 2021). Bathymetric data for Southeast Kyushu show a seafloor reentrant structure corresponding to the shadow zone that was formed by subduction of the Kyushu–Palau Ridge (Park et al., 2009).

Sandbox modeling indicates that both the accretionary wedge and forearc basin are uplifted in response to seamount subduction (Dominguez et al., 2000) and similar phenomena have been observed in some subduction zones (e.g., Fleury et al., 2009; Sak et al., 2009). Subduction and underplating of seamounts could cause the localized uplift and seaward tilting of slope deposits in the forearc region (Sak et al., 2009), similar to the study area (Figs. 2 and 3).

Therefore, the subducting Kyushu–Palau Ridge is the most plausible origin of the unique uplift in the study area. The wide variations in consolidation of the three lithofacies in the Miyazaki Group reflected differences in the depositional environment and amount of regional uplift in South Kyushu.

6. Conclusions

Analyses of the calcareous nannofossil stratigraphy and physical properties (porosity, paleo-temperature, and maximum effective stress) of Neogene sediments in the Miyazaki forearc basin have led to the following conclusions.

- The lower parts of the Aoshima (Gonoharu Formation) and Miyazaki (Tano and Aya formations) facies are newly assigned to NN11 and CN9.
- The sediments of the Miyazaki Group show large spatial variations in physical properties (porosity, paleo-temperature, and consolidation yield stress), despite having similar depositional ages (late Miocene–Pliocene).
- The tops of the Aoshima and Miyazaki facies show a minor difference in maximum paleo-temperature (10–20°C) but a large difference in consolidation yield stress (<20 MPa). This indicates that mechanical consolidation due to maximum effective stress was the dominant control on lithification in the Miyazaki forearc basin, rather than depositional age or maximum temperature.
- There is a large difference in maximum burial depth between the Aoshima (>3500 m) and Miyazaki facies (<1600 m), despite the minor difference in the depositional ages (5–6 Ma). The differences in the maximum burial depth (ΔD_{max} >2000 m) represent variations in sedimentary environments in the Miyazaki Group.
- The large amount of uplift apparently occurred in association with the counter-clockwise

block rotation of South Kyushu and/or subduction of the Kyushu–Palau Ridge, making distribution of the highly consolidated sedimentary rocks only in the southern Miyazaki Group.

Acknowledgements

Part of this study was supported by two JSPS Research Grants (19H02008 and 21K18178) awarded to Yuzuru Yamamoto and 22H01587 awarded to Feng Zhang. We thank Drs. Takehiro Hirose, Osamu Tadai and Takahiro Suzuki for assistance of specimen preparations at the Kochi Institute for Core Sample Research of the Japan Agency for Marine-Earth Science and Technology. We are grateful to Dr. Stephen Bowden and other members of the laboratory for discussing and improving this manuscript. Two anonymous reviewers are acknowledged for their constructive comments, which improved the manuscript.

References

Ask, V. S., Kopf, A., 2004. Constraints on the state of in situ effective stress and the mechanical behavior of ODP Leg 186 claystones in the Japan Trench forearc. The Island Arc, 13, 242–257. https://doi.org/10.1111/j.1440-1738.2003.00423.x

Barker, C. E., 1983. Influence of time on metamorphism of sedimentary organic matter in liquid-dominated geothermal systems, western North America. Geology, 7, 384-388. https://doi.org/10.1130/0091-7613(1983)11<384:IOTOMO>2.0.CO;2

Blow, W. H., 1969. Late middle Eocene to Recent planktonic foraminiferal biostratigraphy. Proc. 1st Intern.Conf. Plank Microfossils, 1, 199-421.

Bown, P. R., Young, J. R., 1998. Techniques. In: Bown, P.R. (Ed.), Calcareous Nannofossils Biostratigraphy. Chapman and Hall (Kluwer Academic Publishers), Dordrecht, pp. 16–28. https://doi.org/10.1007/978-94-011-4902-0_2

503 Casagrande, A., 1936. The Determination of the Pre-Consolidation Load and Its Practical
504 Significance. Proceedings of the 1st International Conference on Soil Mechanics,
505 Harvard, 3, 3-60.
506 Chiyonobu, S., Torii, M., Morimoto, J., Oda, M., 2011. Pliocene/Pleistocene boundary and
507 paleoceanographic significance of the upper Miyazaki Group, southern Kyushu,
508 Southwest Japan, based on calcareous nannofossil and planktic foraminiferal
509 assemblages. The Journal of the Geological Society of Japan, 2, 109-116. (in Japanese
510 with English abstract) https://doi.org/10.5575/geosoc.2011.0011
511 Cornard, P. H., Moernaut, J., Moore, G. F., Kioka, A., Kopf, A., Ferreira C. S., Strasser, M.,
512 2022. Sequence stratigraphic evolution of the Kumano forearc basin during the last
513 deglaciation: Influence of eustasy and tectonically-controlled shelf morphology on deep-
514 marine sediment dynamics. Sedimentary Geology, 430, 106100.
515 https://doi.org/10.1016/j.sedgeo.2022.106100
516 Dominguez, S., Malavieille, J., Lallemand, S.E., 2000. Deformation of accretionary wedges in
517 response to seamount subduction: Insights from sandbox experiments. Tectonics, 1, 182-
518 196. https://doi.org/10.1029/1999TC900055
519 Endo, H., Suzuki, Y. 1986. Geology of the Tsuma and Takanabe district. Quadrangle series scale
520 1:50,000 Kagoshima (15), (68 and 69), Geological Survey of Japan, 97 pp. + 4 pp. (in
521 Japanese with English abstract)
522 Franklin, J.A., 1979. Suggest Methods for Determining Water Content, Porosity, Density,
523 Absorption and Related Properties and Swelling and Slake-Durability Index Properties.
524 International Journal of Rock Mechanics and Mining Science & Geomechanics Abstracts,
525 16, 141-156.

526 Fleury, J.M., Pubellier, M., de Urreiztieta, M., 2009. Structural expression of forearc crust uplift
527 due to subducting asperity. Lithos 113 (1–2), 318–330.
528 https://doi.org/10.1016/j.lithos.2009.07.007.
529 Goto, S., Suzuki, K., 2011. The Diagenesis and Compression Strength of the Miyazaki Group.
530 Journal of the Japan Society of Engineering Geology, 4, 143-148. (in Japanese with
531 English abstract) https://doi.org/10.5110/jjseg.52.143
532 Ishihara, Y., Abe, H., Oshikawa, M., 2009. Sediment gravity flow deposits and specificity of
533 stratigraphic patterns in the Neogene Aoshima Formation, Miyazaki Group, Nichinan
534 Coast, SW Japan. Journal of the Sedimentological Society of Japan, 2, 65-84. (in
535 Japanese with English abstract) https://doi.org/10.4096/jssj.67.65
536 Jaky, J., 1944. The coefficient of earth pressure at rest. In Hungarian A nyugalmi nyomas
537 tenyezoje. J. Soc. Hung. Eng. Arch. (Magyar Mernok es Epitesz-Egylet Kozlonye), 355–
538 358.
539 Janbu, N., 1969. The resistance concept applied to deformation of soils. In: Proceedings of the
540 7th international conference of soil mechanics and foundation engineering, 1, 191–196.
541 Japanese Standards Association, 2009a. Test Method for one-Dimensional Consolidation
542 Properties of Soils Using Constant Rate of Strain Loading. JIS a 1227: 2009. pp. 1–9 (in
543 Japanese).
544 Japanese Standards Association, 2009b. Test Method for one-Dimensional Consolidation
545 Properties of Soils Using Incremental Loading. JIS a 1217: 2009. pp. 1–13 (in Japanese).
546 Kagiyama, T., 1994. Kirishima volcanoes-Multi active volcanic Group generated in a slightly
547 tensile stress field: Journal of Geography, 103, 479–487. (in Japanese with English
548 abstract) https://doi.org/10.5026/jgeography.103.5_479

549 Kamiya, N., Yamamoto, Y., Wang, Q., Kurimoto, Y., Zhang, F., Takemura, T., 2017. Major
550 variations in vitrinite reflectance and consolidation characteristics within a post-middle
551 Miocene forearc basin, central Japan: A geodynamical implication for basin evolution.
552 Tectonophysics, 710-711, 69-80. https://doi.org/10.1016/j.tecto.2016.10.027
553 Kamiya, N., Yamamoto, Y., Zhang, F., Lin, W., 2020a. Vitrinite reflectance and consolidation
554 characteristics of the post-middle Miocene Forearc Basin in central and eastern Boso
555 Peninsula, central Japan: Implications for basin subsidence. Island Arc, e12344.
556 https://doi.org/10.1111/iar.12344
557 Kamiya, N., Zhang, F., Fukuoka, J., Kato, Y. and Lin, W., 2020b. Strain Softening of Siltstones
558 in Consolidation Process. Mechanics of Materials, 6, 1096-1101.
559 https://doi.org/10.2320/matertrans.Z-M2020818
560 Kino, Y., 1959. Geological map of Japan: Hyuga-Aoshima. Quadrangle series scale 1:50,000
561 Kagoshima (84) Geological Survey of Japan. (in Japanese with English abstract)
562 Kino, Y., Kageyama, K., Okumura, K., Endo, H., Fukuta, O., Ykoyama, S., 1984. Geology of
563 the Miyazaki district. Quadrangle series scale 1:50,000 Kagoshima (15), (76), Geological
564 Survey of Japan, 94 pp. + 4 pp. (in Japanese with English abstract)
565 Kodama, K., Nakayama, K., 1993. Paleomagnetic evidence for post-Late Miocene intra-arc
566 rotation of South Kyushu, Japan. Tectonics, 12, 35-47.
567 https://doi.org/10.1029/92TC01712
568 Kodama, K., Tashiro, H., Takeuchi, T., 1995. Quaternary counterclockwise rotation of south
569 Kyushu, southwest Japan. Geology, 9, 823-826. https://doi.org/10.1130/0091-
570 7613(1995)023<0823:QCROSK>2.3.CO;2
571 Lin, W., Hirose, T., Tadai, O., Tanikawa, W., Ishitsuka, K., Yang, X., 2020. Thermal
572 conductivity profile in the Nankai accretionary prism at IODP NanTroSEIZE Site C0002:

573 Estimations from high-pressure experiments using input site sediments.
574 Geochemistry,Geophysics, Geosystems, 21, e2020GC009108.
575 https://doi.org/10.1029/2020GC009108
576 Maemoku, H., 1992. Holocene Tectonic Movements in the Southern Part of the Outer Zone of
577 Southwest Japan. Quaternary Research, 5, 285-296. (in Japanese with English abstract)
578 https://doi.org/10.4116/jaqua.31.285
579 Mahony, S.H., Wallace, L.M., Miyoshi, M., Villamor, P., Sparks, R.S.J., Hasenaka, T., 2011.
580 Volcano-tectonic interactions during rapid plate-boundary evolution in the Kyushu region,
581 SW Japan. *GSA Bulletin*, 123 (11-12): 2201–2223. https://doi.org/10.1130/B30408.1
582 Martini, E., 1971. Standard Tertiary and Quaternary Calcareous Nannoplankton
583 Zonation.Proceedings of the 2nd Planktonic Conference, Roma, 1970, 739-785.
584 Menant, A., Angiboust, S., Gerya, T., Lacassin, R., Simoes, M., Grandin, R., 2020. Transient
585 stripping of subducting slabs controls periodic forearc uplift. *Nat Commun* **11**, 1823.
586 https://doi.org/10.1038/s41467-020-15580-7
587 Nagaoka, S., Maemoku, H., Matsushita, Y., 1991. Evolution of Holocene Coastal Landforms in
588 the Miyazaki Plain, Southern Japan. Quaternary Research, 2, 59-78. (in Japanese with
589 English abstract) https://doi.org/10.4116/jaqua.30.59
590 Nagaoka, S., Nishiyama, K., Inoue, Y., 2010. Geologic and Geomorphologic Evolution of
591 Miyazaki Plain in Southern Japan during the Past 2 Ma, Based on the Sea-level Change
592 and Tectonics. Journal of Geography, 4, 632-667. (in Japanese with English abstract)
593 https://doi.org/10.5026/jgeography.119.632
594 Nakamura. Y., Ozawa, T., Nobuhara, T., 1999. Stratigraphy and molluscan fauna of the upper
595 Miocene to lower Pliocene Miyazaki Group in the Aoshima area, Miyazaki Prefecture,

596 southwest Japan. The Journal of the Geological Society of Japan, 1, 45-60. (in Japanese
597 with English abstract) https://doi.org/10.5575/geosoc.105.45
598 Nawa, K., Murata, Y., Komazawa, M., Morijiri, R., Hiroshima, T., Makino, M., Murakami, F.,
599 Kisimoto, K., Okuma, S., Shichi, R., 2005. Bouguer Gravity Anomalies in Miyazaki
600 District, Kyushu, Japan. Bulletin of the geological survey of Japan, 5-6, 183-208.
601 https://doi.org/10.9795/bullgsj.56.183
602 Nielsen, S. B., Clausen, O. R., McGregor, E., 2017. basin%Ro : A vitrinite reflectance model
603 derived from basin and laboratory data. Basin Research, 29, S1, 515–536.
604 https://doi.org/10.1111/bre.12160
605 Oda, M., Chiyonobu, S., Torii, M., Otomo, T., Morimoto, J., Satou, Y., Ishikawa, H., Ashikawa,
606 M., Tominaga, O., 2011. Integrated magneto-biochronology of the Pliocene-Pleistocene
607 Miyazaki succession, southern Kyushu, southwest Japan: Implications for an Early
608 Pleistocene hiatus and defining the base of the Gelasian (P/P boundary type section) in
609 Japan. Journal of Asian Earth Sciences., 40, 84-97,
610 https://doi.org/10.1016/j.jseaes.2010.09.003
611 Okada, H., Bukry, D., 1980. Supplementary modification and introduction of code numbers to the
612 low-latitude coccolith biostratigraphic zonation (Bukry, 1973; 1975). Marine
613 Micropaleontology, 5, 321–325. https://doi.org/10.1016/0377-8398(80)90016-X
614 Park, J. O., Hori, T., Kaneda, Y., 2009. Seismotectonic implications of the Kyushu-Palau Ridge
615 subducting beneath the westernmost Nankai forearc. Earth, Planets and Space, 61, 1013-
616 1018. https://doi.org/10.1186/BF03352951
617 Prakash, K., Sridharan, A., 2020. Log–Log Method of Pre-consolidation/Yield Stress
618 Determination: An Appraisal. Geotechnical and Geological Engineering, 38, 947-959.
619 https://doi.org/10.1007/s10706-019-01030-9

620 Raffi, I., Backman, J., Fornaciari, E., Palike, H., Rio, D., Lourens, L., Hilgen, F., 2006. A review
621 of calcareous nannofossil astrobiochronology encompassing the past 25 million years.
622 Quaternary Science Review, 25, 3113–3137.
623 https://doi.org/10.1016/j.quascirev.2006.07.007
624 Sak, P. B., Fisher, D. M., Gardner, T. W., Marshall, J. S., LaFemina, P. C., 2009. Rough crust
625 subduction, forearc kinematics, and Quaternary uplift rates, Costa Rican segment of the
626 Middle American Trench. *GSA Bulletin*, 121 (7-8): 992–1012.
627 https://doi.org/10.1130/B26237.1
628 Scholl, D. W., 2021. Seismic imaging evidence that forearc underplating built the accretionary
629 rock record of coastal North and South America. *Geological Magazine*, 158: 104–117.
630 https://doi.org/10.1017/ S0016756819000955.
631 Sridharan, A., Abraham, B. M., Jose, B. T., 1991. Improved technique for estimation of
632 preconsolidation pressure. Géotechnique, 2, 263-268.
633 https://doi.org/10.1680/geot.1991.41.2.263
634 Steinmetz, J.C., 1979. Calcareous nannofossils from the North Atlantic Ocean, Leg 49, Deep
635 Sea Drilling Project. In: Luyendyk, B.P., Cann, J.R., et al. (Eds.), Initial Reports DSDP
636 49.U.S. Govt. Printing Office, Washington:pp, 519–531
637 http://dx.doi.org/10.2973/dsdp.proc.49.116.1979.
638 Shuto, T., 1952. The geohistorical study of the Miyazaki Group. Science Reports of the Kyushu
639 University, Geology, 4, 1–40. (in Japanese with English abstract)
640 Shuto, T., 1961. Palaeontological Study of the Miyazaki Group: A General Account of Faunas.
641 Kyushu University, Series D, Geology, 2, 73-206. https://doi.org/10.5109/1526109
642 Strasser, M., Dugan, B., Kanagawa, K., Moore, G.F., Toczko, S., Maeda, L., Kido, Y., Moe,
643 K.T., Sanada, Y., Esteban, L., Fabbri, O., Geersen, J., Hammerschmidt, S., Hayashi, H.,

644 Heirman, K., Hüpers, A., Jurado Rodriguez, M.J., Kameo, K., Kanamatsu, T., Kitajima,
645 H., Masuda, H., Milliken, K., Mishra, R., Motoyama, I., Olcott, K., Oohashi, K.,
646 Pickering, K.T., Ramirez, S.G., Rashid, H., Sawyer, D., Schleicher, A., Shan, Y., Skarbek,
647 R., Song, I., Takeshita, T., Toki, T., Tudge, J., Webb, S., Wilson, D.J., Wu, H.-Y., and
648 Yamaguchi, A., 2014. Site C0002. In Strasser, M., Dugan, B., Kanagawa, K., Moore,
649 G.F., Toczko, S., Maeda, L., and the Expedition 338 Scientists, Proc. IODP, 338:
650 Yokohama (Integrated Ocean Drilling Program).
651 https://doi:10.2204/iodp.proc.338.103.2014
652 Suzuki, H., 1987. Stratigraphy of the Miyazaki Group in the southeastern part of Miyazaki
653 Prefecture, Kyushu, Japan. Contributions from the Institute of Geology and Paleontology
654 Tohoku University 90, 1–24 (in Japanese with English abstract).
655 Sweeney, J. J., Burnham, A. K., 1990. Evaluation of a simple model of vitrinite reflectance
656 based on chemical kinetics. The American Association of Petroleum Geologists Bulletin,
657 74(10), 1559-1570. https://doi.org/10.1306/0C9B251F-1710-11D7-8645000102C1865D
658 Tahara, M., Uehira, K., Shimizu, H., Nakada, M., Yamada, T., Mochizuki, K., Shinohara, M.,
659 Nishino, M., Hino, R., Yakiwara, H., Miyamachi, H., Umakoshi, K., Goda, M., Matsuwo,
660 N., Kanazawa, T, 2008. Seismic velocity structure around the Hyuganada region,
661 Southwest Japan, derived from seismic tomography using land and OBS data and its
662 implications for interplate coupling and vertical crustal uplift. Physics of the Earth and
663 Planetary Interiors, 167(1-2), https://doi.org/19-33. 10.1016/j.pepi.2008.02.001
664 Takashimizu, T., 2009. Ancient submarine-canyon system developed within forearc basin fill,
665 Mio-Pliocene “Miyazaki facies & rdquo: Miyazaki Group, western Japan. Geological
666 Survey of Japan, 11, 559-577. (in Japanese with English abstract)
667 https://doi.org/10.5575/geosoc.115.559

668 Tobin, H., Hirose, T., Saffer, D., Toczko, S., Maeda, L., Kubo, Y., Boston, B., Broderick, A.,
669 Brown, K., Crespo-Blanc, A., Even, E., Fuchida, S., Fukuchi, R., Hammerschmidt, S.,
670 Henry, P., Josh, M., Jurado, M.J., Kitajima, H., Kitamura, M., Maia, A., Otsubo, M.,
671 Sample, J., Schleicher, A., Sone, H., Song, C., Valdez, R., Yamamoto, Y., Yang, K.,
672 Sanada, Y., Kido, Y., and Hamada, Y., 2015. Site C0002. In Tobin, H., Hirose, T., Saffer,
673 D., Toczko, S., Maeda, L., Kubo, Y., and the Expedition 348 Scientists, Proc. IODP, 348:
674 College Station, TX (Integrated Ocean Drilling Program).
675 https://doi:10.2204/iodp.proc.348.103.2015
676 Torii, M., Oda, M., Itaya, T., 2000. K-Ar Dating of Tuff Beds Intercalated in the Miyazaki
677 Group, Kyushu, Japan. Bulletin of the Volcanological Society of Japan, 3, 131-148. (in
678 Japanese with English abstract) https://doi.org/10.18940/kazan.45.3_131
679 Uehara, S., Tamura, Y., Marumo, H., and Mitsuhashi, S., 2016. Estimation of maximum burial
680 depth of Neogene-Quaternary fore-arc basin formation based on laboratory porosity
681 measurements. Tectonophysics, https://doi.org/677–678, 241-247.
682 10.1016/j.tecto.2016.04.004
683 Ujiie, K., and Oki, K., 1993. On the Stratigraphic and Structural Relationship between the
684 Miyazaki and the Aoshima Facies of the upper Neogene Miyazaki Group, Kyushu, Japan.
685 Reports of the Faculty of Science, Kagoshima University (Geology, Biology), 26, 67-84.
686 (in Japanese with English abstract)
687 Velde, B., 1996. Compaction trends of clay-rich deep sea sediments. Marine Geology, 133, 193-
688 201. https://doi.org/10.1016/0025-3227(96)00020-5
689 Xia, C., Zheng, Y., Liu, B., Hua, Q., Ma, L., Li, X., Xie, Q., 2021. Tectonic implications of the
690 subduction of the Kyushu-Palau Ridge beneath the Kyushu, southwest Japan. Acta
691 Oceanol. Sin. 40, 70–83 (2021). https://doi.org/10.1007/s13131-021-1711-8

692 Yamaji, A., 2003. Slab rollback suggested by latest Miocene to Pliocene forearc stress and
693 migration of volcanic front in southern Kyushu, northern Ryukyu Arc. Tectonophysics,
694 364, 9-24. https://doi .org /10.1016/S0040-1951(03)00047-7
695 Yamamoto, Y., Hamada, Y., Kamiya, N., Ojima, C., Chiyonobu, S., Saito, S., 2017. Geothermal
696 structure of the Miura–Boso plate subduction margin, central Japan. Tectonophysics, 710-
697 711, 81-87. https://doi.org/10.1016/j.tecto.2016.11.004
698 Yamamoto, Y., Obana, K., Takahashi, T., Nakanishi, A., Kodaira, S., Kaneda, Y., 2013. Imaging
699 of the subducted Kyushu-Palau Ridge in the Hyuga-nada region, west-ern Nankai Trough
700 subduction zone. Tectonophysics589, 90–102. https://doi .org /10 .1016
701 /j .tecto .2012 .12 .028.
702 Zhang, J., Chen, L., Cheng, Z., Tang, L., 2020. Geological characteristics of the Nankai Trough
703 subduction zone and their tectonic significances. Acta Oceanologica Sinica, 10, 81-95.
704 https://doi.org/10.1007/s13131-020-1663-4
705

706 **Figure captions**

707 **Fig. 1.** (a) Plate configuration map of the islands of Japan. PAP = Pacific Plate, PSP = Philippine
708 Sea Plate, NAP = North American Plate, and ERP = Eurasian Plate. The red-colored rectangle
709 indicates the area covered by Figs 1b, 2, and 7. (b) Geological map of the Miyazaki area. The
710 red dotted line shows the inferred fault between the Aoshima and Miyazaki facies (Kagiyama,
711 1994; Kodama et al., 1995).
712

713 **Fig. 2.** (a) Detailed geological map of the northern half of the Miyazaki Group (after Kino et al.,
714 1984; Endo and Suzuki, 1986). (b) Detailed geological map of the southern half of the Miyazaki
715 Group (after Nakamura et al., 1999). Legends are listed in Fig. 2c. Yellow circles indicate

716 sampling locations. V and CS correspond to samples for vitrinite reflectance analysis (MyV)
717 and consolidation tests (MyCS), respectively. (c) Stratigraphy of the Miyazaki Group including
718 the spatial distribution of three lithofacies. The figure shows the ages of the Aoshima (after
719 Kino, 1959; Ujiie and Oki, 1993; Nakamura et al., 1999), Miyazaki (after Kino et al., 1984;
720 Endo and Suzuki, 1986; Suzuki, 1987; Ujiie and Oki, 1993; Takashimizu, 2009), and Tsuma
721 (after Kino et al., 1984; Endo and Suzuki, 1986; Suzuki, 1987; Torii et al., 2000; Oda et al.,
722 2011) facies. Gp. = Group and Fm. = Formation.
723
724 **Fig. 3.** Stereoplot diagrams showing poles to bedding planes in the study area (lower-
725 hemisphere equal-area projections). Black circles show the confidence intervals ($\alpha = 95$). (a)
726 Aoshima Facies. (b) Miyazaki Facies. (c) Tsuma Facies.
727
728 **Fig. 4.** Stratigraphic columnar section of the Miyazaki Group with depositional age, vitrinite
729 reflectance (R_O) and consolidation yield stress (p_c) identified in this study. Black circles show
730 stratigraphic sampling locations for the vitrinite reflectance (V) and consolidation tests (CS). *:
731 age data after Ujiie and Oki (1993). Black arrow indicates north direction.
732
733 **Fig. 5.** Initial porosity and grain density of the siltstones used for consolidation tests. Orange =
734 Aoshima Facies, green = Miyazaki Facies, and blue = Tsuma Facies. The porosity decreases
735 gradually from top to bottom of each lithofacies. Sandy siltstones (MyCS2, MyCS3, MyCS5, and
736 MyCS6) have relatively low porosities in each lithofacies. The Aoshima Facies is characterized
737 by a lower porosity in the Miyazaki Group. Black arrows indicate samples with the same
738 depositional age (MyCS4, MyCS12, MyCS16, MyCS18, and MyCS20).
739

740 **Fig. 6.** Histograms of vitrinite reflectance data for the Miyazaki area. M/T: boundary between
741 the Miyazaki/Tsuma facies. A/M: boundary between the Aoshima/Miyazaki facies.
742
743 **Fig. 7.** Distribution of vitrinite reflectance values in the Miyazaki area. Circle colors indicate R_O
744 (%). The accretionary complex is characterized by high values of vitrinite reflectance (0.8%–
745 1.0%). In the forearc basin, the vitrinite reflectance of the Aoshima Facies is relatively high
746 (0.4%–0.7%), whereas that of the Tsuma Facies is low (0.3%–0.5%). Vitrinite reflectance
747 increases gradually from top to bottom in each lithofacies.
748
749 **Fig. 8.** Consolidation curves for each sample. (a–c) Results for the Tsuma Facies. (d–e) Results
750 for the Miyazaki Facies. (f) Results for the Aoshima Facies.
751
752 **Fig.9.** (a) Relationship between depositional age and porosities for the Miyazaki Group. Black
753 arrows indicate samples with the same depositional age (MyCS4, MyCS5, MyCS12, MyCS16,
754 MyCS18, and MyCS20). The depositional age of each sample is provided in Table A3. (b)
755 Depositional ages and paleo temperatures calculated from vitrinite reflectance data. (c)
756 Depositional ages and consolidation yield stress. (d) Depositional ages and Maximum burial
757 depth. (e) Porosity and consolidation yield stress. The siltstone porosity decreases linearly with
758 increasing p_c. (f) Porosity and paleo temperature. There is a minor increase in paleo temperature
759 with decreasing porosity. (g) Consolidation yield stress and paleo temperature.
760
761 **Fig. 10.** Schematic model of the evolution of the Miyazaki Group. (a) Sedimentation of the
762 Miyazaki Group. Open arrows indicate the direction of sediment supply (Ishihara et al., 2009;
763 Takashimizu, 2009). The Aoshima Facies accumulated on the deep-sea floor, as compared with

764 the Miyazaki Facies. The Tsuma Facies started to accumulate at the same time as the upper parts
765 of the Aoshima and Miyazaki facies, and are interbedded. (b) Last stage of sedimentation of the
766 Miyazaki Group. Numbers indicate the maximum burial depth for each formation. The middle–
767 upper part of the Tsuma Facies above the Uryuno Formation conformably overlies the upper
768 Miyazaki Facies. (c) Subduction of the Kyushu–Palau Ridge and counter-clockwise rotation of
769 the South Kyushu microplates (after Kodama et al., 1995). The boundary between microplates A
770 and B corresponds to the boundary between the Miyazaki and Aoshima facies. PSP = Philippine
771 Sea Plate, ERP = Eurasian Plate, KPR = Kyushu–Palau Ridge, and OT = Okinawa Trough. (d)
772 Uplift of the Aoshima Facies caused by rotation of the South Kyushu microplates and
773 subduction of the Kyushu–Palau Ridge. The red dotted line shows the inferred fault dividing the
774 Aoshima and Miyazaki facies (Kagiyama, 1994; Kodama et al., 1995). (e) Present-day
775 distributions of the three lithofacies.
776
777 **Fig. A1.** (a) Schematic diagram showing void ratio (e) versus the log of confining stress. Open
778 circles indicate the consolidation yield stress (p_c), which corresponds to the maximum effective
779 stress experienced by the sample. (b) Calculation method for p_c proposed by Sridharan (1991).
780 The consolidation curve is plotted on a log–log diagram showing specific volume ($1+e$) and
781 consolidation stress. Lines 1 and 2 represent the linear parts of the consolidation curve. The p_c
782 value is defined as the point of intersection of the two straight lines.
783
784 **Fig. A2.** (a) Consolidation curves for low-porosity siltstones (MyCS4 from the Aoshima
785 Formation). Two samples yielded similar consolidation curves. The p_c values of MyCS4-1 and
786 MyCS4-2 are 38.4 and 37.5 MPa, respectively. (b) Consolidation curves for two samples
787 (MyCS1 and MyCS2) that did not yield clear consolidation yield points.

788

789 **Table 1.** Occurrences of calcareous nannofossils in the Miyazaki Group.

790

791 **Table 2.** Porosity, grain density, and consolidation yield stress (p_c) of the siltstones, and

792 calculated maximum burial depths (D_{max}) for the Miyazaki Group.

793

794 **Table 3.** Vitrinite reflectance data (R_O) and paleo-temperatures obtained from R_O values based

795 on EASY% R_O (Sweeney and Burnham, 1990). M/T: boundary between the Miyazaki/Tsuma

796 facies. A/M: boundary between the Aoshima/Miyazaki facies.

797

798 **Table A1.** Heating time for each formation, as used to calculate the maximum paleo-

799 temperature. The depositional ages are based on Suzuki (1987), Ujiie and Oki (1993),

800 Nakamura et al. (1999), Torii et al. (2000), and Oda et al. (2011). We assumed that heating in the

801 entire Miyazaki forearc basin continued until *ca*. 2.2 Ma, corresponding to the Hisamine

802 unconformity.

803

804 **Table A2.** Calculation of D_{max} values for each lithofacies. The n value is the ratio of pore space

805 to the solid part of each sample. The mean (n) is the mean value of the upper and lower

806 formations of the overburden. (a) Tsuma Facies. (b) Miyazaki Facies. The Ikime Formation is

807 overlain by the middle–upper Tsuma Facies (i.e., above the Uryuno Formation). (c) Aoshima

808 Facies. The Aoshima Formation is overlain by the middle–upper Tsuma Facies (i.e., above the

809 Uryuno Formation).

810

811 **Table A3.** Depositional age of each sample shown in Fig. 9. The ages are based on Suzuki
812 (1987), Ujiie and Oki (1993), Nakamura et al. (1999), Torii et al. (2000), Oda et al. (2011), and
813 this study.

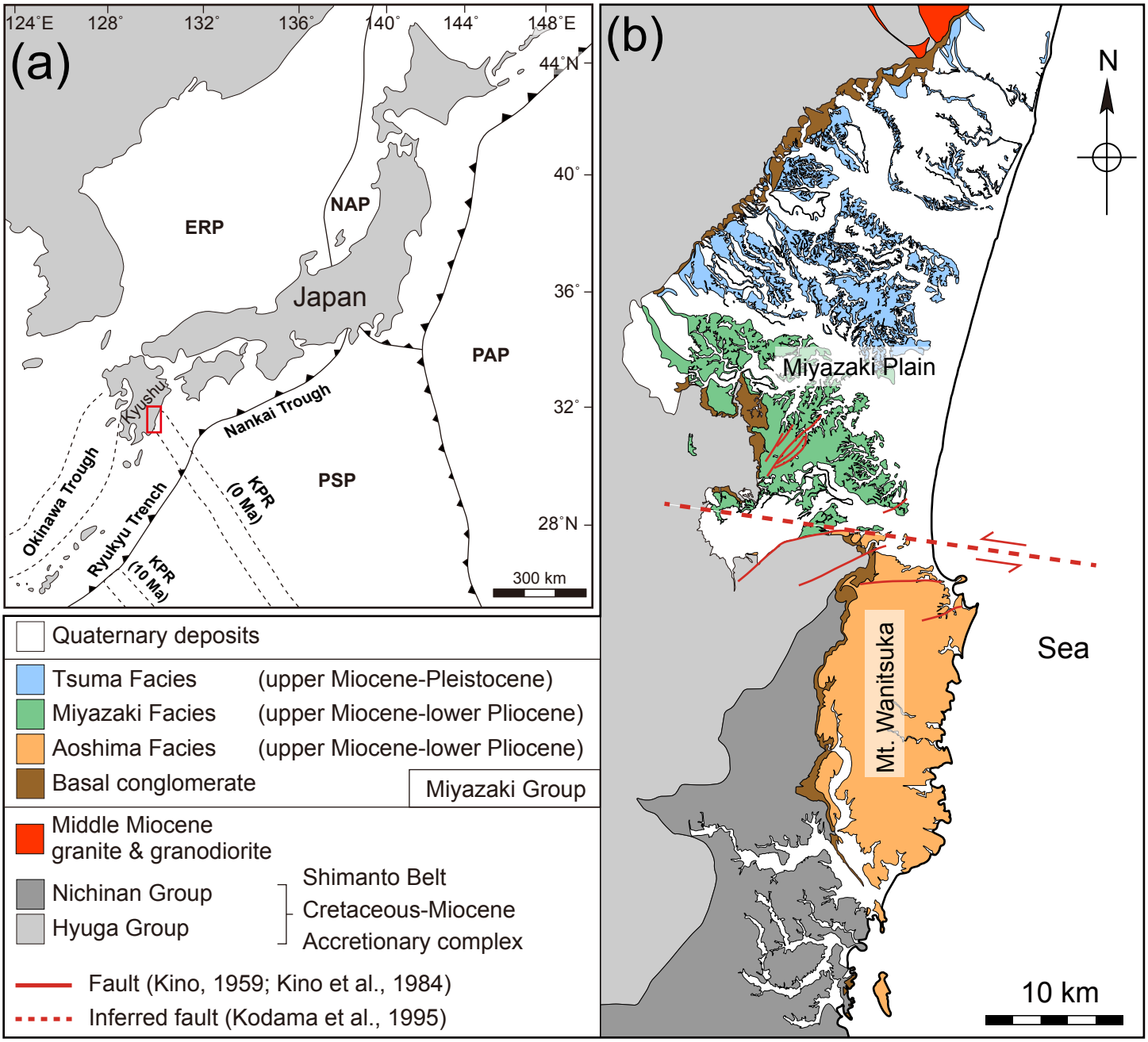

Fig. 1. (a) Plate configuration map of the islands of Japan. PAP = Pacific Plate, PSP = Philippine Sea Plate, NAP = North American Plate, and ERP = Eurasian Plate, KPR = Kyushu–Palau Ridge. The red-colored rectangle indicates the area covered by Figs 1b, 2, and 7. (b) Geological map of the Miyazaki area. The red dotted line shows the inferred fault between the Aoshima and Miyazaki facies (Kagiyama, 1994; Kodama et al., 1995).

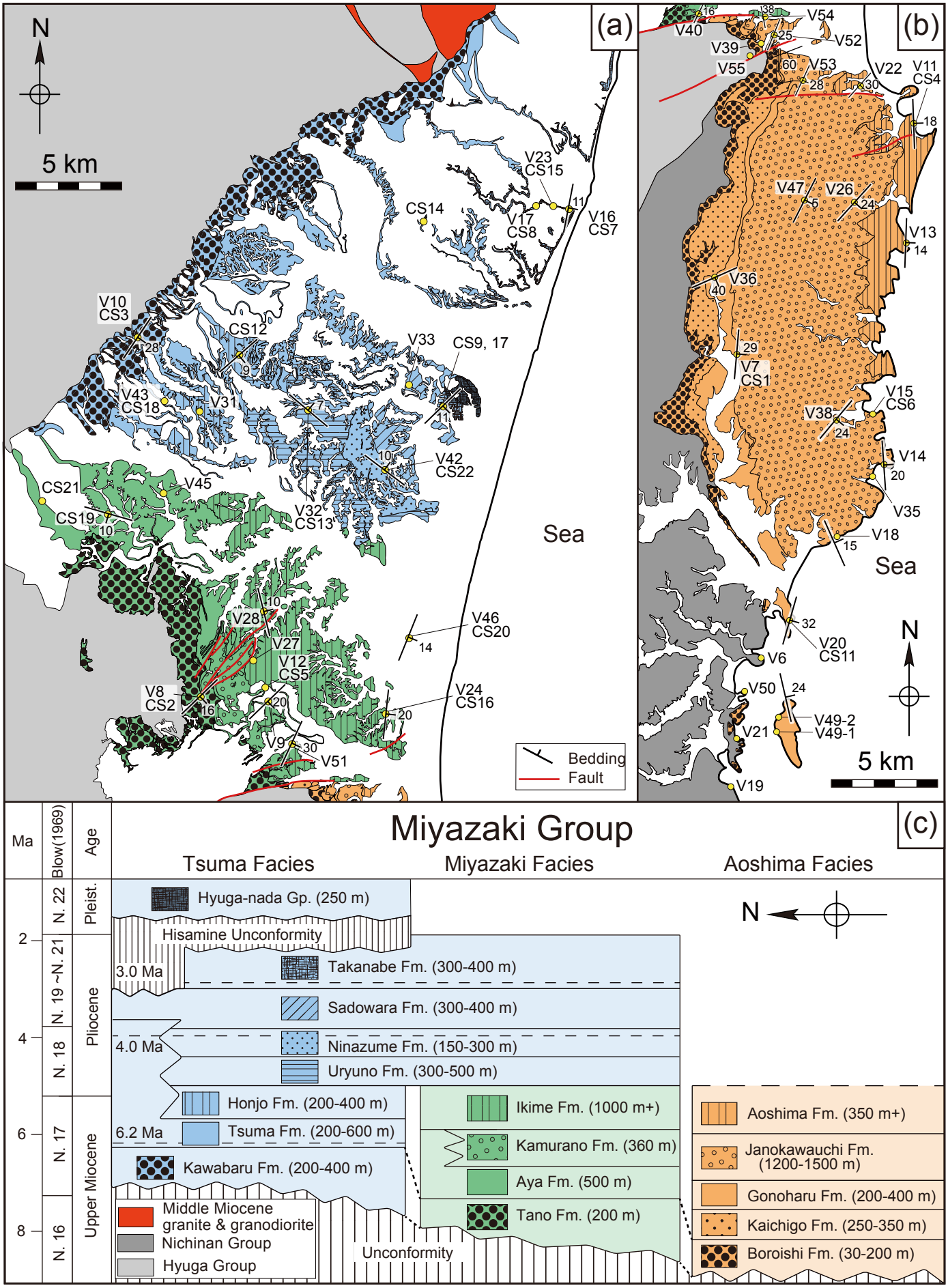

Fig. 2. (a) Detailed geological map of the northern half of the Miyazaki Group (after Kino et al., 1984; Endo and Suzuki, 1986). (b) Detailed geological map of the southern half of the Miyazaki Group (after Nakamura et al., 1999). Legends are listed in Fig. 2c. Yellow circles indicate sampling locations. V and CS correspond to samples for vitrinite reflectance analysis (MyV) and consolidation tests (MyCS), respectively. (c) Stratigraphy of the Miyazaki Group including the spatial distribution of three lithofacies. The figure shows the ages of the Aoshima (after Kino, 1959; Ujiie and Oki, 1993; Nakamura et al., 1999), Miyazaki (after Kino et al., 1984; Endo and Suzuki, 1986; Suzuki, 1987; Ujiie and Oki, 1993; Takashimizu, 2009), and Tsuma (after Kino et al., 1984; Endo and Suzuki, 1986; Suzuki, 1987; Torii et al., 2000; Oda et al., 2011) facies. Gp. = Group and Fm. = Formation.

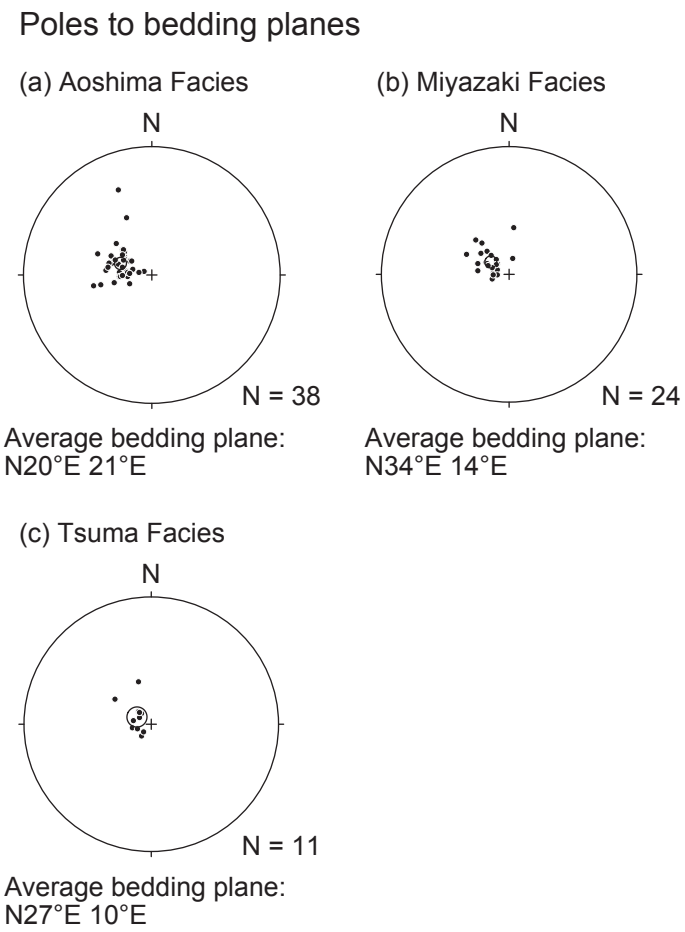

Fig. 3. Stereoplot diagrams showing poles to bedding planes in the study area (lower-hemisphere equal-area projections). Black circles show the confidence intervals (α = 95). (a) Aoshima Facies. (b) Miyazaki Facies. (c) Tsuma Facies.

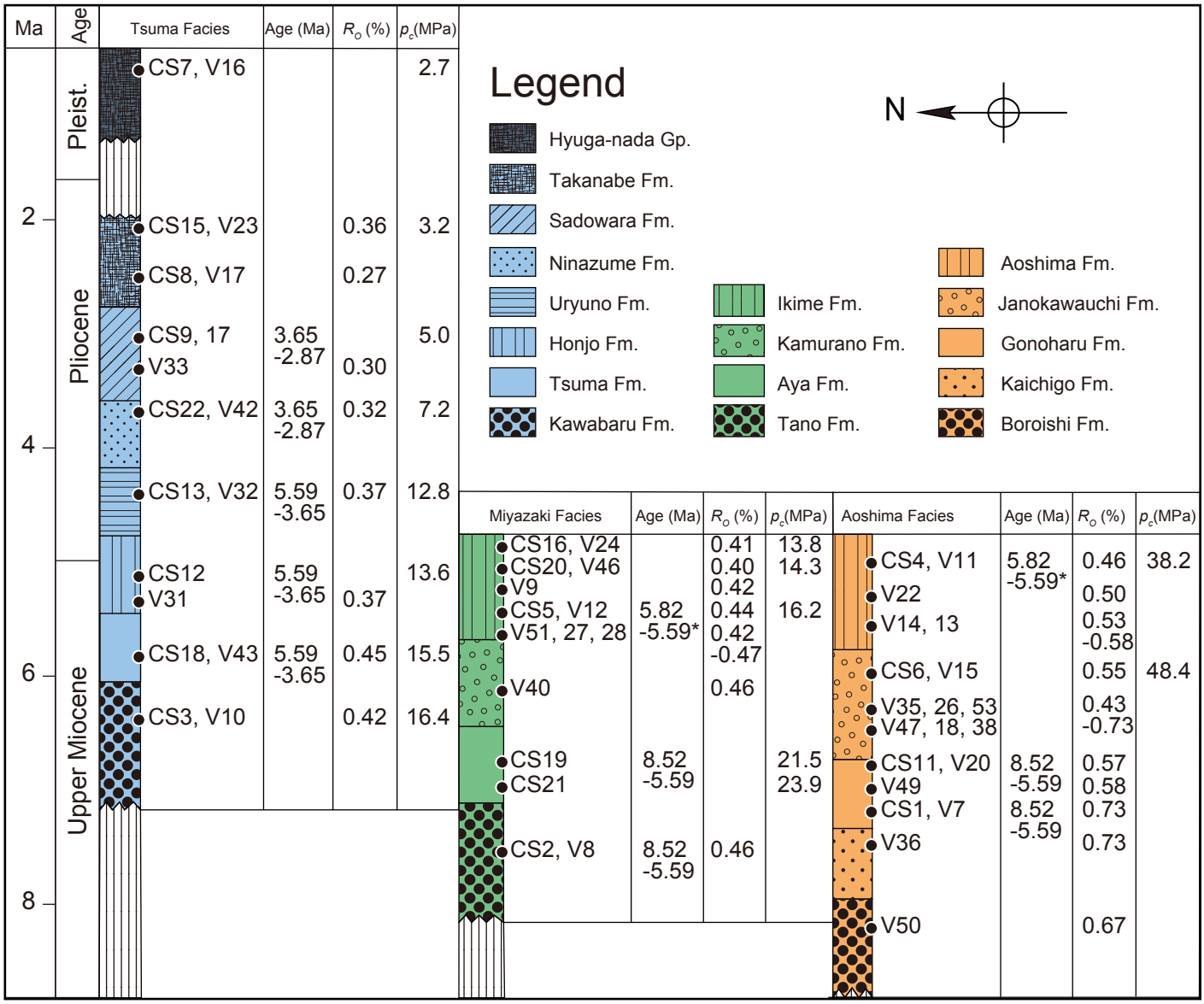

Fig. 4. Stratigraphic columnar section of the Miyazaki Group with depositional age, vitrinite reflectance (R_o) and consolidation yield stress (p_c) identified in this study. Black circles show stratigraphic sampling locations for the vitrinite reflectance (V) and consolidation tests (CS). Black arrow indicates north direction. *: age data after Ujiie and Oki (1993). Black arrow indicates north direction.

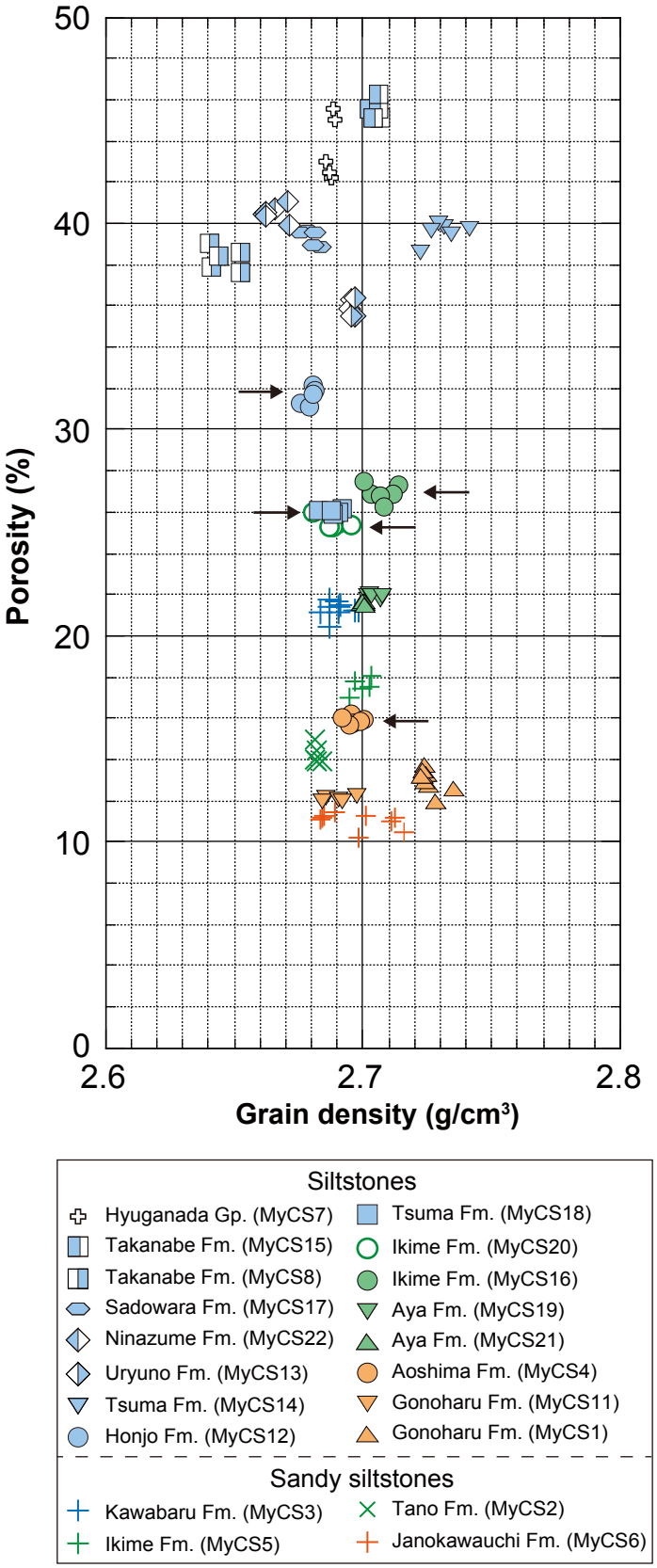

Fig. 5. Initial porosity and grain density of the siltstones used for consolidation tests. Orange = Aoshima Facies, green = Miyazaki Facies, and blue = Tsuma Facies. The porosity decreases gradually from top to bottom of each lithofacies. Sandy siltstones (MyCS2, MyCS3, MyCS5, and MyCS6) have relatively low porosities in each lithofacies. The Aoshima Facies is characterized by a lower porosity in the Miyazaki Group. Black arrows indicate samples with the same depositional age (MyCS4, MyCS12, MyCS16, MyCS18, and MyCS20).

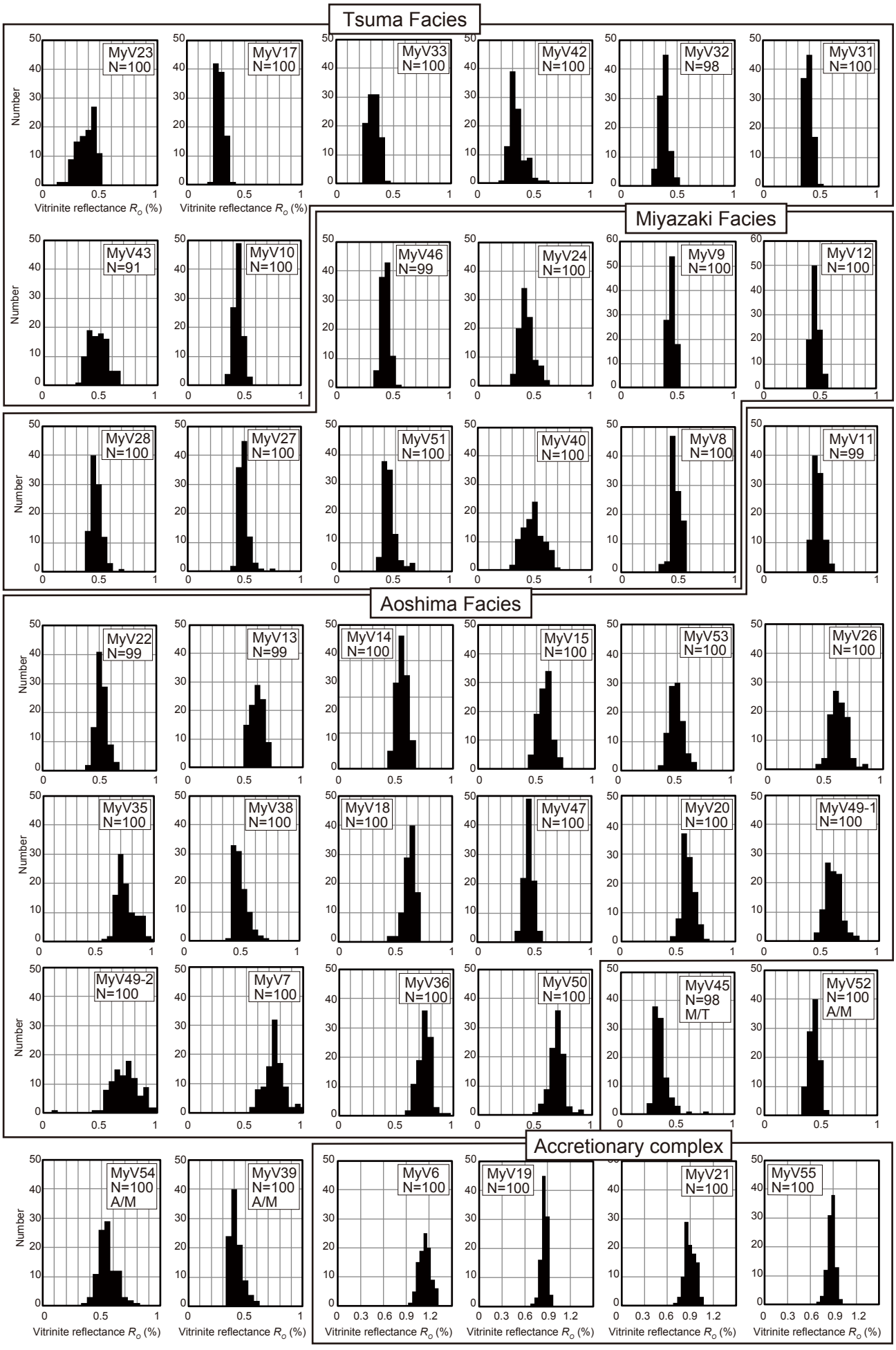

Fig. 6. Histograms of vitrinite reflectance data for the Miyazaki area.M/T: boundary between the Miyazaki/Tsuma facies. A/M: boundary between the Aoshima/Miyazaki facies.

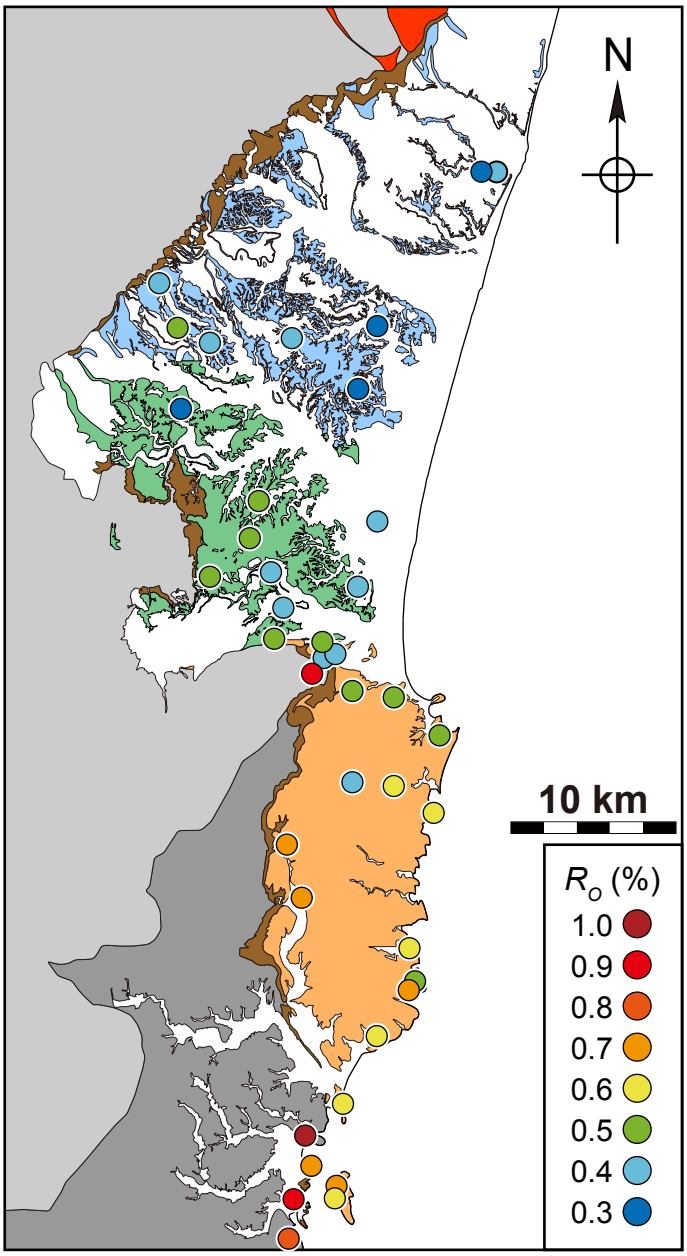

Fig. 7. Distribution of vitrinite reflectance values in the Miyazaki area. Circle colors indicate R_o (%). The accretionary complex is characterized by high values of vitrinite reflectance (0.8%–1.0%). In the forearc basin, the vitrinite reflectance of the Aoshima Facies is relatively high (0.4%–0.7%), whereas that of the Tsuma Facies is low (0.3%–0.5%). Vitrinite reflectance increases gradually from top to bottom in each lithofacies.

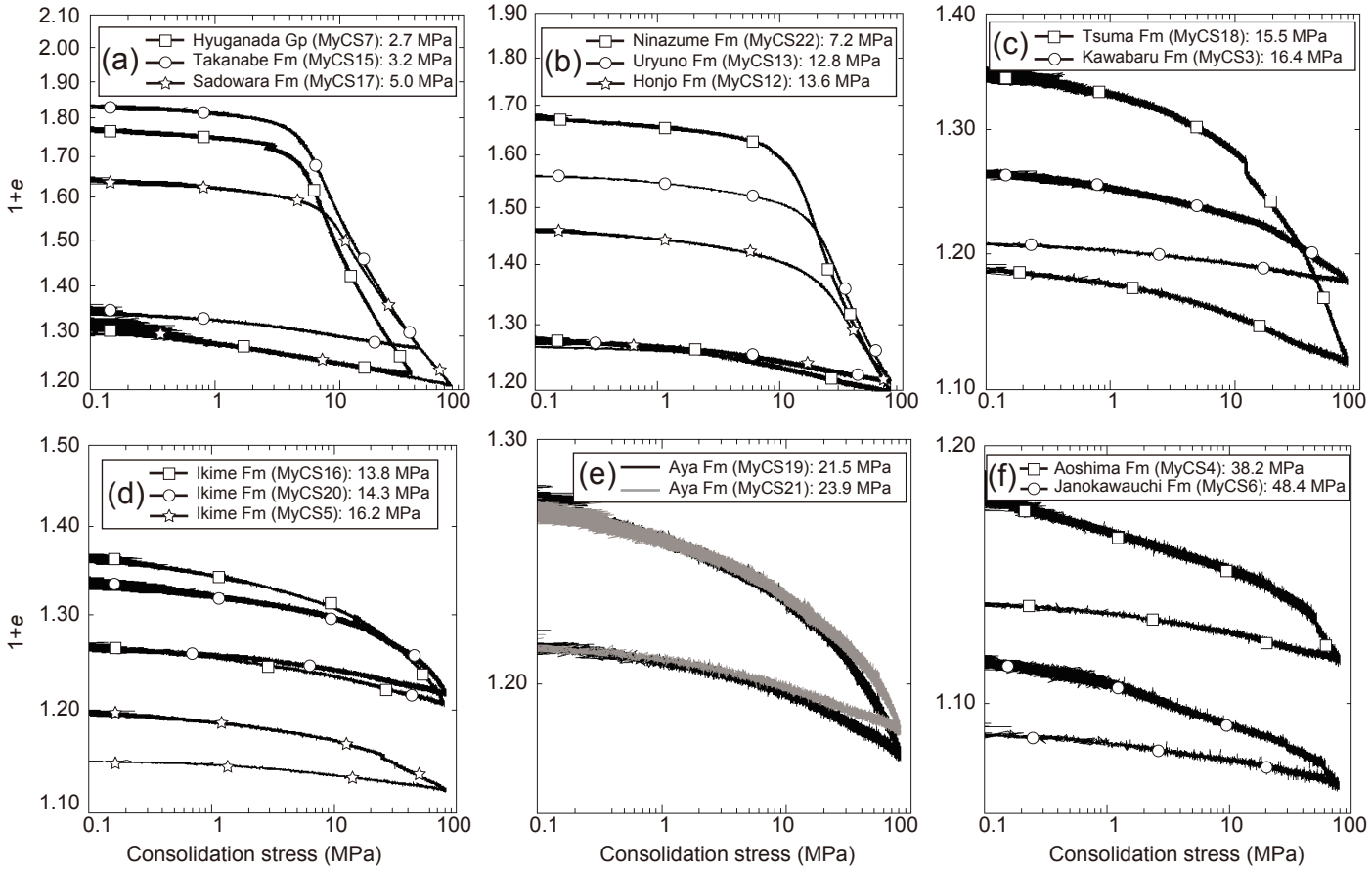

Fig. 8. Consolidation curves for each sample. (a–c) Results for the Tsuma Facies. (d–e) Results for the Miyazaki Facies. (f) Results for the Aoshima Facies.

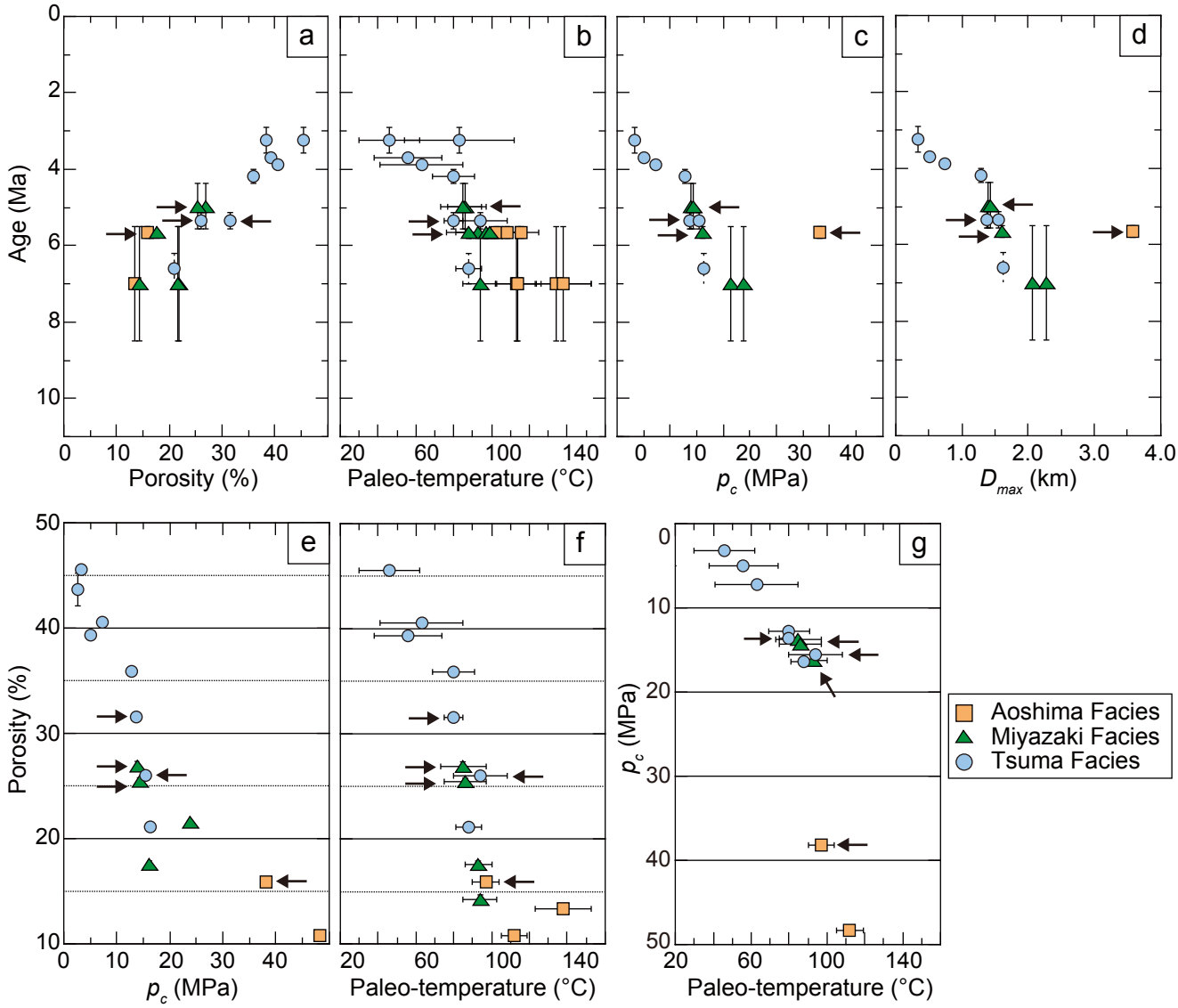

Fig. 9. (a) Relationship between depositional age and porosities for the Miyazaki Group. Black arrows indicate samples with the same depositional age (MyCS4, MyCS5, MyCS12, MyCS16, MyCS18, and MyCS20). The depositional age of each sample is provided in Table A3. (b) Depositional ages and paleo temperatures calculated from vitrinite reflectance data. (c) Depositional ages and consolidation yield stress. (d) Depositional ages and Maximum burial depth. (e) Porosity and consolidation yield stress. The siltstone porosity decreases linearly with increasing p_c. (f) Porosity and paleo temperature. There is a minor increase in paleo-temperature with decreasing porosity. (g) Consolidation yield stress and paleo temperature.

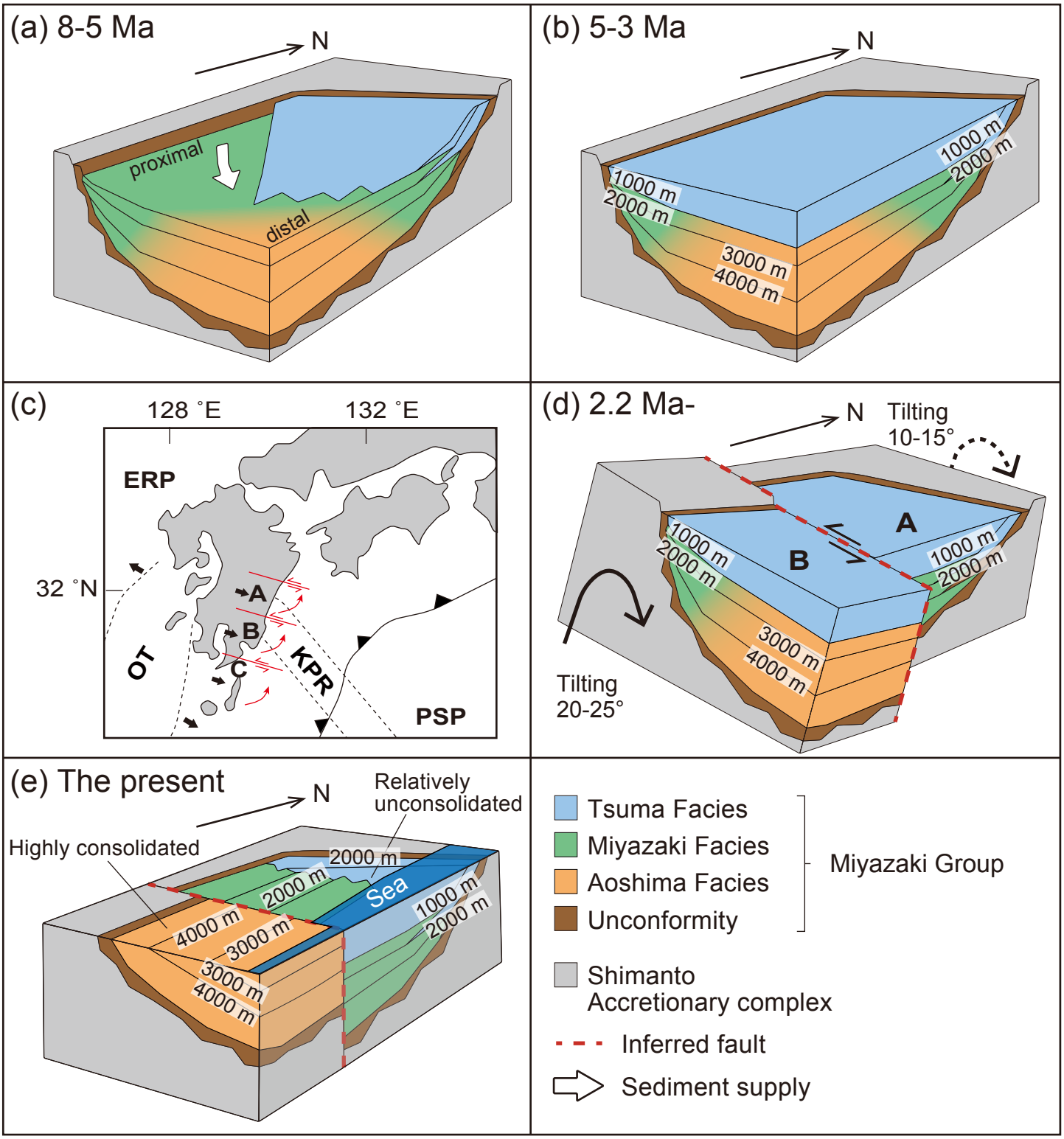

Fig. 10. Schematic model of the evolution of the Miyazaki Group. (a) Sedimentation of the Miyazaki Group. Open arrows indicate the direction of sediment supply (Ishihara et al., 2009; Takashimizu, 2009). The Aoshima Facies accumulated on the deep-sea floor, as compared with the Miyazaki Facies. The Tsuma Facies started to accumulate at the same time as the upper parts of the Aoshima and Miyazaki facies, and are interbedded. (b) Last stage of sedimentation of the Miyazaki Group. Numbers indicate the maximum burial depth for each formation. The middle–upper part of the Tsuma Facies above the Uryuno Formation conformably overlies the upper Miyazaki Facies. (c) Counter-clockwise rotation of the South Kyushu microplates (after Kodama et al., 1995). The boundary between microplates A and B corresponds to the boundary between the Miyazaki and Aoshima facies. PSP = Philippine Sea Plate, ERP = Eurasian Plate, KPR = Kyushu–Palau Ridge, and OT = Okinawa Trough. (d) Uplift of the Aoshima Facies potentially caused by rotation of the South Kyushu microplates and subduction of the Kyushu–Palau Ridge. The red dotted line shows the inferred fault dividing the Aoshima and Miyazaki facies (Kagiyama, 1994; Kodama et al., 1995). (e) Present-day distributions of the three lithofacies.

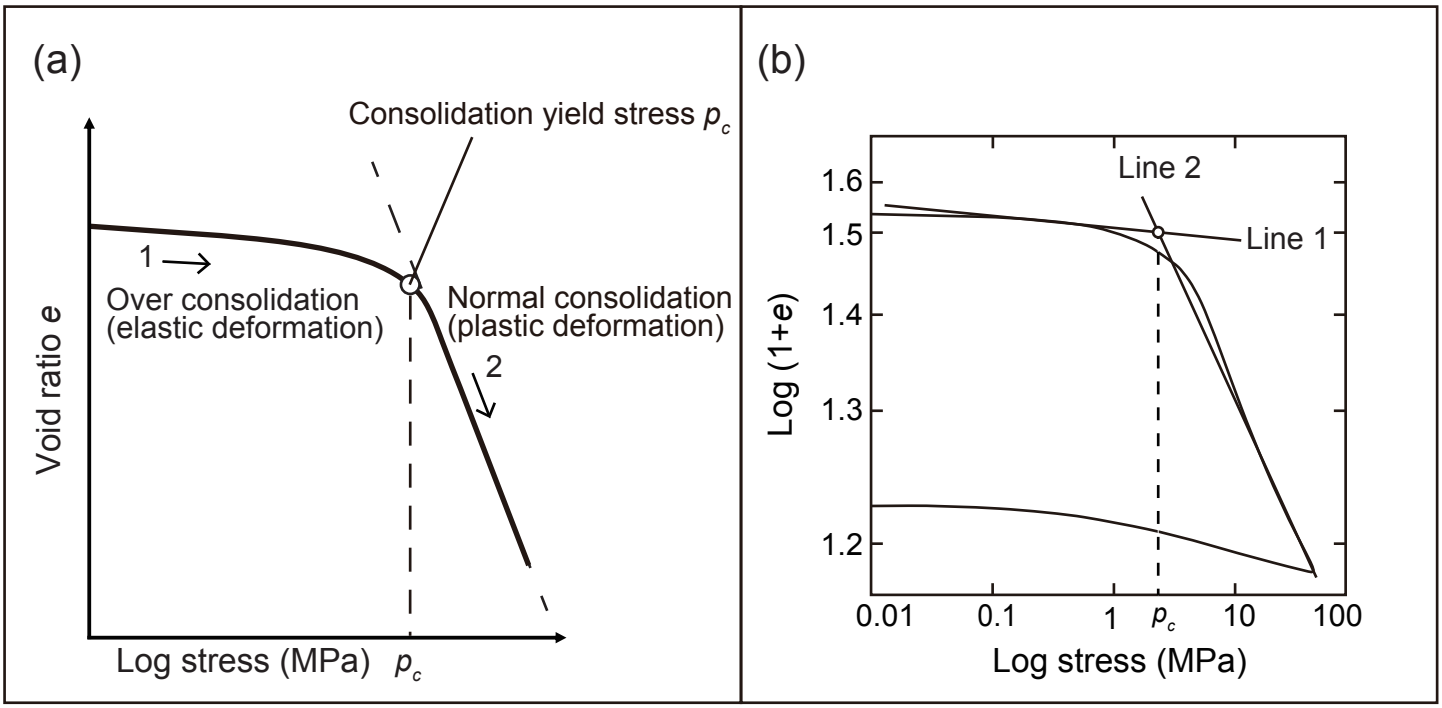

Fig. A1. (a) Schematic diagram showing void ratio (*e*) versus the log of confining stress. Open circles indicate the consolidation yield stress (p_c), which corresponds to the maximum effective stress experienced by the sample. (b) Calculation method for p_c proposed by Sridharan (1991). The consolidation curve is plotted on a log–log diagram showing specific volume (1+*e*) and consolidation stress. Lines 1 and 2 represent the linear parts of the consolidation curve. The p_c value is defined as the point of intersection of the two straight lines.

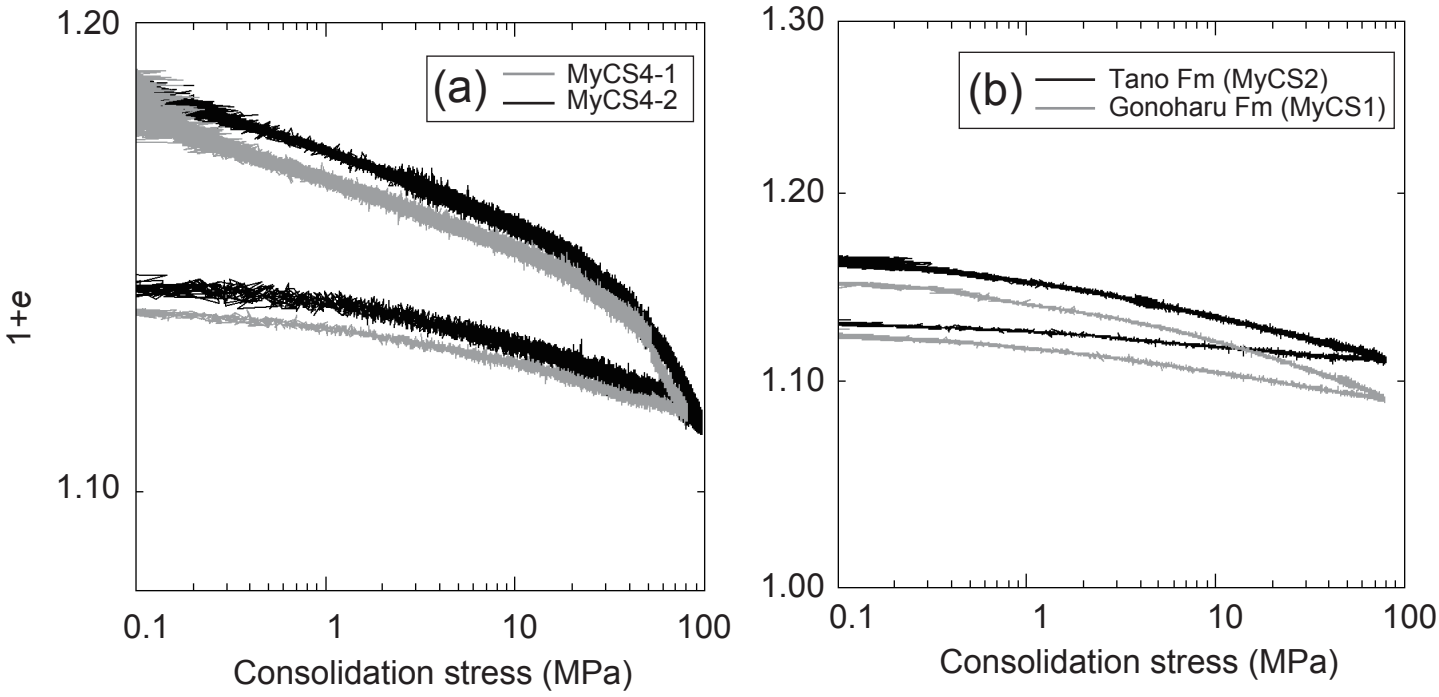

Fig. A2. (a) Consolidation curves for low-porosity siltstones (MyCS4 from the Aoshima Formation). Two samples yielded almost the same consolidation curve. p_c values of MyCS4-1 and 4-2 are 38.4 and 37.5 MPa, respectively.
(b) Consolidation curves for two samples (MyCS1 and MyCS2) that did not yield clear consolidation yield points.

	Preservation	*Discoaster berggrenii*	*Discoaster brouweri*	*Discoaster pentaradiatus*	*Discoaster quinqueramus*	*Discoaster surculus*	*Discoaster tamalis*	*Gephyrocapsa spp. (<4 μm)*	*Reticulofenestra pseudoumbilicus*	*Sphenolithus abies*
MyCS1	P	+		+	+				+	+
MyCS2-2	P	+							+	+
MyCS8	P							+		
MyCS9	P		+	+		+	+			
MyCS11	P	+		+	+				+	+
MyCS12-2	P		+	+		+	+		+	+
MyCS13	M		+	+		+	+		+	+
MyCS14	M		+	+		+	+		+	+
MyCS17	M		+	+		+	+			
MyCS18	P		+	+			+		+	+
MyCS19	P	+			+				+	+
MyCS22	P		+	+			+			

Table 1. Occurrences of calcareous nannofossils in the Miyazaki Group.

(Single-column)

Sample ID	Facies	Formation	Porosity (%)	Grain density (g/cm^3)	p_c (MPa)	D_{max} (m)
MyCS7	Tsuma	Higoyashiki	43.7 ± 1.5	2.69	2.7	280
MyCS15	Tsuma	Takanabe	45.5 ± 0.5	2.70	3.2	330
MyCS17	Tsuma	Sadowara	39.3 ± 0.4	2.68	5.0	510
MyCS22	Tsuma	Ninazume	40.5 ± 0.4	2.67	7.2	740
MyCS13	Tsuma	Uryuno	35.9 ± 0.4	2.70	12.8	1290
MyCS12	Tsuma	Honjo	31.6 ± 0.4	2.68	13.6	1370
MyCS18	Tsuma	Tsuma	26.1 ± 0.1	2.69	15.5	1550
MyCS3	Tsuma	Kawabaru	21.1 ± 0.4	2.69	16.4	1630
MyCS16	Miyazaki	Ikime	26.9 ± 0.4	2.71	13.8	1390
MyCS20	Miyazaki	Ikime	25.5 ± 0.3	2.69	14.3	1430
MyCS5	Miyazaki	Ikime	17.5 ± 0.4	2.70	16.2	1600
MyCS19	Miyazaki	Aya	21.9 ± 0.1	2.70	21.5	2060
MyCS21	Miyazaki	Aya	21.6 ± 0.1	2.70	23.9	2270
MyCS2	Miyazaki	Tano	14.3 ± 0.5	2.68	---	---
MyCS4	Aoshima	Aoshima	15.9 ± 0.2	2.70	38.2	3590
MyCS6	Aoshima	Janokawauchi	10.8 ± 0.4	2.70	48.4	4430
MyCS11	Aoshima	Gonoharu	12.1 ± 0.1	2.69	---	---
MyCS1	Aoshima	Gonoharu	13.4 ± 0.2	2.72	---	---

Table 2. Porosity, grain density, and consolidation yield stress (p_c) of the siltstones, and calculated maximum burial depths (D_{max}) for the Miyazaki Group. (2-column)

Sample ID	Facies	Formation	R_O (%)	Paleo-temperature (°C)
MyV23	Tsuma	Takanabe	0.36 ± 0.08	83 ± 29
MyV17	Tsuma	Takanabe	0.27 ± 0.04	46 ± 16
MyV33	Tsuma	Sadowara	0.30 ± 0.05	56 ± 18
MyV42	Tsuma	Ninazume	0.32 ± 0.07	63 ± 22
MyV32	Tsuma	Uryuno	0.37 ± 0.05	80 ± 11
MyV31	Tsuma	Honjo	0.37 ± 0.03	80 ± 5
MyV43	Tsuma	Tsuma	0.45 ± 0.08	94 ± 14
MyV10	Tsuma	Kawabaru	0.42 ± 0.04	88 ± 7
MyV46	Miyazaki	Ikime	0.41 ± 0.04	86 ± 9
MyV24	Miyazaki	Ikime	0.40 ± 0.06	85 ± 12
MyV9	Miyazaki	Ikime	0.42 ± 0.03	88 ± 7
MyV12	Miyazaki	Ikime	0.44 ± 0.04	93 ± 7
MyV28	Miyazaki	Ikime	0.46 ± 0.05	97 ± 8
MyV27	Miyazaki	Ikime	0.47 ± 0.05	99 ± 8
MyV51	Miyazaki	Ikime	0.42 ± 0.06	88 ± 12
MyV40	Miyazaki	Kamurano	0.46 ± 0.09	96 ± 15
MyV8	Miyazaki	Tano	0.46 ± 0.05	94 ± 9
MyV11	Aoshima	Aoshima	0.46 ± 0.05	97 ± 7
MyV11-2	Aoshima	Aoshima	0.47 ± 0.04	98 ± 6
MyV22	Aoshima	Aoshima	0.50 ± 0.06	103 ± 10
MyV13	Aoshima	Aoshima	0.58 ± 0.06	116 ± 9

MyV14	Aoshima	Aoshima	0.53 ± 0.05	108 ± 7
MyV15	Aoshima	Janokawauchi	0.55 ± 0.06	112 ± 7
MyV53	Aoshima	Janokawauchi	0.47 ± 0.06	98 ± 10
MyV26	Aoshima	Janokawauchi	0.60 ± 0.07	118 ± 13
MyV35	Aoshima	Janokawauchi	0.73 ± 0.09	140 ± 13
MyV38	Aoshima	Janokawauchi	0.45 ± 0.07	94 ± 9
MyV18	Aoshima	Janokawauchi	0.61 ± 0.05	119 ± 10
MyV47	Aoshima	Janokawauchi	0.43 ± 0.04	90 ± 6
MyV20	Aoshima	Gonoharu	0.57 ± 0.06	113 ± 11
MyV49-1	Aoshima	Gonoharu	0.58 ± 0.07	114 ± 12
MyV49-2	Aoshima	Gonoharu	0.70 ± 0.14	134 ± 19
MyV7	Aoshima	Gonoharu	0.73 ± 0.09	138 ± 15
MyV36	Aoshima	Kaichigo	0.73 ± 0.06	137 ± 10
MyV50	Aoshima	Boroishi	0.67 ± 0.07	129 ± 10
MyV45		M/T	0.33 ± 0.07	--
MyV52		A/M	0.42 ± 0.04	--
MyV54		A/M	0.53 ± 0.08	--
MyV39		A/M	0.40 ± 0.06	--
MyV6		Nichinan Gp.	1.12 ± 0.08	--
MyV19		Nichinan Gp.	0.84 ± 0.04	--
MyV21		Nichinan Gp.	0.88 ± 0.07	--
MyV55		Nichinan Gp.	0.86 ± 0.05	--

Table 3. Vitrinite reflectance data (R_O) and paleo-temperatures obtained from R_O values based on EASY% R_O (Sweeney and Burnham, 1990). M/T: boundary between the Miyazaki/Tsuma facies. A/M: boundary between the Aoshima/Miyazaki facies. (2-column)

Sample ID	Facies	Formation	Heating time (Ma)	Reference
MyV23	Tsuma	Takanabe	3.0-2.2	Oda et al. (2011)
MyV17	Tsuma	Takanabe	3.0-2.2	Oda et al. (2011)
MyV33	Tsuma	Sadowara	3.5-2.2	Torii et al. (2000); Oda et al. (2011)
MyV42	Tsuma	Ninazume	4.0-2.2	Suzuki (1987); Torii et al. (2000)
MyV32	Tsuma	Uryuno	4.0-2.2	Suzuki (1987); Torii et al. (2000)
MyV31	Tsuma	Honjo	5.0-2.2	Suzuki (1987)
MyV43	Tsuma	Tsuma	6.0-2.2	Suzuki (1987)
MyV10	Tsuma	Kawabaru	6.5-2.2	Torii et al. (2000)
MyV46	Miyazaki	Ikime	5.5-2.2	Ujiie and Oki (1993)
MyV24	Miyazaki	Ikime	5.5-2.2	Ujiie and Oki (1993)
MyV9	Miyazaki	Ikime	5.5-2.2	Ujiie and Oki (1993)
MyV12	Miyazaki	Ikime	5.5-2.2	Ujiie and Oki (1993)
MyV28	Miyazaki	Ikime	5.5-2.2	Ujiie and Oki (1993)
MyV27	Miyazaki	Ikime	5.5-2.2	Ujiie and Oki (1993)
MyV51	Miyazaki	Ikime	5.5-2.2	Ujiie and Oki (1993)
MyV40	Miyazaki	Kamurano	6.0-2.2	Ujiie and Oki (1993)
MyV8	Miyazaki	Tano	8.0-2.2	This study
MyV11	Aoshima	Aoshima	5.5-2.2	Ujiie and Oki (1993)
MyV11-2	Aoshima	Aoshima	5.5-2.2	Ujiie and Oki (1993)
MyV22	Aoshima	Aoshima	5.5-2.2	Ujiie and Oki (1993)
MyV13	Aoshima	Aoshima	5.5-2.2	Ujiie and Oki (1993)

MyV14	Aoshima	Aoshima	5.5-2.2	Ujiie and Oki (1993)
MyV15	Aoshima	Janokawauchi	6.0-2.2	Nakamura et al. (1999)
MyV53	Aoshima	Janokawauchi	6.0-2.2	Nakamura et al. (1999)
MyV26	Aoshima	Janokawauchi	6.0-2.2	Nakamura et al. (1999)
MyV35	Aoshima	Janokawauchi	6.0-2.2	Nakamura et al. (1999)
MyV38	Aoshima	Janokawauchi	6.0-2.2	Nakamura et al. (1999)
MyV18	Aoshima	Janokawauchi	6.0-2.2	Nakamura et al. (1999)
MyV47	Aoshima	Janokawauchi	6.0-2.2	Nakamura et al. (1999)
MyV20	Aoshima	Gonoharu	7.0-2.2	This study
MyV49-1	Aoshima	Gonoharu	7.0-2.2	This study
MyV49-2	Aoshima	Gonoharu	7.0-2.2	This study
MyV7	Aoshima	Gonoharu	7.0-2.2	This study
MyV36	Aoshima	Kaichigo	8.0-2.2	Nakamura et al. (1999)
MyV50	Aoshima	Boroishi	8.0-2.2	Nakamura et al. (1999)
MyV45		M/T	--	--
MyV52		A/M	--	--
MyV54		A/M	--	--
MyV39		A/M	--	--
MyV6		Nichinan Gp.	--	--
MyV19		Nichinan Gp.	--	--
MyV21		Nichinan Gp.	--	--
MyV55		Nichinan Gp.	--	--

Table A1. Heating time for each formation, as used to calculate the maximum paleo-temperature. The depositional ages are based on Suzuki (1987), Ujiie and Oki (1993), Nakamura et al. (1999), Torii et al. (2000), and Oda et al. (2011). We assumed that heating in the entire Miyazaki forearc basin continued until *ca*. 2.2 Ma, corresponding to the Hisamine unconformity.

(a) Sample ID	p_c (MPa)	n	Mean (n)	ρ_{bulk} (g/cm^3)	Δp_c (MPa)	ΔD (m)	D_{max} (m)
Overburden			0.44	1.96	2.7	281	
MyCS7	2.7	0.44					281
			0.43	1.97	0.5	52	
MyCS15	3.2	0.42					333
			0.41	2.01	1.8	183	
MyCS17	5.0	0.39					516
			0.40	2.02	2.2	222	
MyCS22	7.2	0.41					738
			0.38	2.05	5.6	557	
MyCS13	12.8	0.36					1295
			0.34	2.13	0.8	77	
MyCS12	13.6	0.32					1372
			0.29	2.21	1.9	175	
MyCS18	15.5	0.26					1548
			0.24	2.30	0.9	80	
MyCS3	16.4	0.21					1628

(b) Sample ID	p_c (MPa)	n	Mean (n)	ρ_{bulk} (g/cm^3)	Δp_c (MPa)	ΔD (m)	D_{max} (m)
Overburden			0.44	1.96	2.7	281	
MyCS7	2.7	0.44					281
			0.43	1.97	0.5	52	
MyCS15	3.2	0.42					333
			0.41	2.01	1.8	183	
MyCS17	5.0	0.39					516
			0.40	2.02	2.2	222	
MyCS22	7.2	0.41					738
			0.38	2.05	5.6	557	
MyCS13	12.8	0.36					1295
			0.31	2.17	1.0	94	
MyCS16	13.8	0.27					1390
			0.26	2.25	0.5	45	
MyCS20	14.3	0.25					1435
			0.22	2.33	1.9	166	
MyCS5	16.2	0.18					1601
			0.20	2.36	5.3	457	

MyCS19	21.5	0.22					2058
			0.22	2.33	2.4	210	
MyCS21	23.9	0.22					2269

(c) Sample ID	p_c (MPa)	n	Mean (n)	ρ_{bulk} (g/cm^3)	Δp_c (MPa)	ΔD (m)	D_{max} (m)
Overburden			0.44	1.96	2.7	281	
MyCS7	2.7	0.44					281
			0.43	1.97	0.5	52	
MyCS15	3.2	0.42					333
			0.41	2.01	1.8	183	
MyCS17	5.0	0.39					516
			0.40	2.02	2.2	222	
MyCS22	7.2	0.41					738
			0.38	2.05	5.6	557	
MyCS13	12.8	0.36					1295
			0.26	2.26	25.4	2294	
MyCS4	38.2	0.16					3590
			0.13	2.47	10.2	842	
MyCS6	48.4	0.11					4432

Table A2. Calculation of D_{max} values for each lithofacies. The n value is the ratio of pore space to the solid part of each sample. The mean (n) is the mean value of the upper and lower formations of the overburden. (a) Tsuma Facies. (b) Miyazaki Facies. The Ikime Formation is overlain by the middle–upper Tsuma Facies (i.e., above the Uryuno Formation). (c) Aoshima Facies. The Aoshima Formation is overlain by the middle–upper Tsuma Facies (i.e., above the Uryuno Formation).

Sample ID	Facies	Formation	Depositional age (Ma)	Reference
MyCS8	Tsuma	Takanabe	3.6-2.9	Oda et al. (2011); This study
MyV17	Tsuma	Takanabe	3.6-2.9	Oda et al. (2011); This study
MyV23	Tsuma	Takanabe	3.6-2.9	Oda et al. (2011); This study
MyCS17	Tsuma	Sadowara	3.8-3.6	Suzuki (1987); Oda et al. (2011)
MyV33	Tsuma	Sadowara	3.8-3.6	Suzuki (1987); Oda et al. (2011)
MyCS22	Tsuma	Ninazume	4.0-3.8	Suzuki (1987); Torii et al. (2000)
MyV42	Tsuma	Ninazume	4.0-3.8	Suzuki (1987); Torii et al. (2000)
MyCS13	Tsuma	Uryuno	4.4-4.0	Suzuki (1987); Torii et al. (2000)
MyV32	Tsuma	Uryuno	4.4-4.0	Suzuki (1987); Torii et al. (2000)
MyCS12	Tsuma	Honjo	5.5-5.1	Suzuki (1987)
MyV31	Tsuma	Honjo	5.5-5.1	Suzuki (1987)
MyCS18	Tsuma	Tsuma	5.5-5.1	Suzuki (1987)
MyV43	Tsuma	Tsuma	5.5-5.1	Suzuki (1987)
MyCS3	Tsuma	Kawabaru	6.2-	Torii et al. (2000)
MyV10	Tsuma	Kawabaru	6.2-	Torii et al. (2000)
MyCS16	Miyazaki	Ikime	5.5-4.4	Suzuki (1987)
MyCS20	Miyazaki	Ikime	5.5-4.4	Suzuki (1987)
MyV24	Miyazaki	Ikime	5.5-4.4	Suzuki (1987)
MyV46	Miyazaki	Ikime	5.5-4.4	Suzuki (1987)
MyCS5	Miyazaki	Ikime	5.8-5.5	Ujiie and Oki (1993)
MyV9	Miyazaki	Ikime	5.8-5.5	Ujiie and Oki (1993)

MyV12	Miyazaki	Ikime	5.8-5.5	Ujiie and Oki (1993)
MyV27	Miyazaki	Ikime	5.8-5.5	Ujiie and Oki (1993)
MyV28	Miyazaki	Ikime	5.8-5.5	Ujiie and Oki (1993)
MyV51	Miyazaki	Ikime	5.8-5.5	Ujiie and Oki (1993)
MyCS19	Miyazaki	Aya	8.5-5.5	This study
MyCS21	Miyazaki	Aya	8.5-5.5	This study
MyV8	Miyazaki	Tano	8.5-5.5	This study
MyCS4	Aoshima	Aoshima	5.8-5.5	Ujiie and Oki (1993)
MyV11	Aoshima	Aoshima	5.8-5.5	Ujiie and Oki (1993)
MyV11-2	Aoshima	Aoshima	5.8-5.5	Ujiie and Oki (1993)
MyV13	Aoshima	Aoshima	5.8-5.5	Ujiie and Oki (1993)
MyV14	Aoshima	Aoshima	5.8-5.5	Ujiie and Oki (1993)
MyV22	Aoshima	Aoshima	5.8-5.5	Ujiie and Oki (1993)
MyCS1	Aoshima	Gonoharu	8.5-5.5	This study
MyV7	Aoshima	Gonoharu	8.5-5.5	This study
MyV20	Aoshima	Gonoharu	8.5-5.5	This study
MyV49-1	Aoshima	Gonoharu	8.5-5.5	This study
MyV49-2	Aoshima	Gonoharu	8.5-5.5	This study

Table A3. Depositional age of each sample shown in Fig. 9. The ages are based on Suzuki (1987), Ujiie and Oki (1993), Nakamura et al. (1999), Torii et al. (2000), Oda et al. (2011), and this study.